Geochimica et Cosmochimica Acta 381 (2024) 223–238

Contents lists available at ScienceDirect

Geochimica et Cosmochimica Acta

journal homepage: www.elsevier.com/locate/gca

The evolution of multiply substituted isotopologues of methane during microbial aerobic oxidation

Jiawen Li [a,*], Beverly K. Chiu [a,1], Alison M. Piasecki [a,2], Xiahong Feng [a], Joshua D. Landis [a], Sarah Marcum [b], Edward D. Young [b], William D. Leavitt [a,c]

[a] Department of Earth Sciences, Dartmouth College, United States
[b] Department of Earth, Planetary, and Space Sciences, UCLA, United States
[c] Department of Chemistry, Dartmouth College, United States

ARTICLE INFO

Associate editor: Shuhei Ono

Dataset link: https://git.dartmouth.edu/leavitt_lab/aerobic_methanotroph, https://figshare.com/projects/Li_etal_2024_AeOM/184504

Keywords:
Aerobic methanotrophy
Clumped isotopes
Methane monooxygenase

ABSTRACT

Aerobic methane oxidation (AeOM) is an important biological sink of methane on Earth. Stable isotopes are critical tools in tracking the sources and sinks of Earth's surface methane budget. However, the major factors that influence the two multiply-substituted (clumped) isotope signatures of AeOM, $\Delta^{13}CH_3D$ and $\Delta^{12}CH_2D_2$, are not well known. Here we quantify the influence of kinetics as a function of temperature and different methane monooxygenase (MMO) enzymes (modulated by copper) on the isotopologue concentrations of residual methane by the obligate aerobic methanotroph, *Methylococcus capsulatus* (Bath). We observe deviations from traditional closed-system distillation (Rayleigh) fractionation during exponential growth at high oxidation rates. We model this as a reservoir effect controlled by the ratio of oxidation rate in the cells to transport rate of methane into the cells, where environmental temperature affects both rates. We also test whether clumped isotope fractionation values vary for the particulate versus soluble MMOs, but the results show minimal differences. We further determine that the back reaction (re-equilibration) of methane with medium water is unlikely. Together, the observations and model demonstrate that at low oxidation-to-transport ratios, the clumped isotope signatures follow canonical Rayleigh fractionation, whereas at high ratios, more positive $\Delta^{12}CH_2D_2$ values result, deviating from simple Rayleigh-like trajectories. This study shows that the methane oxidation-to-transport ratio is a critical influence on clumped isotope signatures of AeOM that should be considered when interpreting the isotopic data of natural methane samples in both open and closed systems.

1. Introduction

Methane is a powerful greenhouse gas that has played a role in Earth's climate for billions of years (Catling et al., 2001; Frieling et al., 2016). Since the Industrial Revolution, methane has accumulated in Earth's atmosphere faster and to a greater extent than any time in at least the last 800 kyr (Ruppel and Kessler, 2017), with significant consequences predicted for extant and future climate (Dlugokencky et al., 2011; Saunois et al., 2020). Methane is also a major component of natural gas, powering vast swaths of the human economy (Hamak and Sigler, 1991; Faramawy et al., 2016). Beyond Earth, the presence and isotopic compositions of methane on other planetary bodies may enable us to differentiate biological from non-biological processes (McKay and Smith, 2005; McKay et al., 2008; Yung et al., 2018; Thompson et al., 2022).

The major sources of methane on Earth include those that are either natural or anthropogenic, as well as biotic or abiotic in origin (Dlugokencky et al., 2011; Kirschke et al., 2013; Saunois et al., 2020). Anthropogenic methane sources include release during fossil fuel extraction, biomass burning, coal mining, agriculture, and waste disposal (i.e. anoxic microbial activity). Natural sources include the microbial degradation of organic matter (e.g. in anoxic wetlands, lakes, oceans, and ruminant guts) and the release of methane from permafrost and gas hydrates. Abiotic methane synthesis is the product of water-rock reactions in hydrothermal systems, including, at lower temperatures, serpentinization (McCollom and Seewald, 2001; Etiope and Sherwood Lollar, 2013). The major methane sinks on Earth include abiotic oxidation in the tropo- and stratosphere due to interactions with OH and Cl radicals (Ehhalt, 1974; Cicerone and Oremland, 1988), as well as microbial oxidation, a.k.a "methanotrophy" (Curry, 2007). Microbial

* Corresponding author.
E-mail address: jiawen.li.gr@dartmouth.edu (J. Li).
[1] Current address: C16 Biosciences, Inc., New York, United States.
[2] Current address: U.S. Geological Survey, Denver, United States.

https://doi.org/10.1016/j.gca.2024.06.032
Received 31 October 2023; Accepted 26 June 2024
Available online 2 July 2024

methanotrophy can be further categorized into the anaerobic oxidation of methane (AOM) and the aerobic oxidation of methane (AeOM). Among them, AeOM plays an important role in methane consumption in peat soils (Oremland and Culbertson, 1992), ocean water (Qin et al., 2022; Mao et al., 2022), and in the atmosphere (Greening and Grinter, 2022). However, there are large discrepancies between top-down and bottom-up estimates of Earth's methane budget (Saunois et al., 2020). In part, this is due to a lack of reliable tools to track the sources and sinks of methane via different pathways.

Methane made and destroyed by abiotic and biological processes possess unique isotopic information that may provide means to identify and track the sources and sinks of methane (Schoell, 1988; Whiticar, 1999; Douglas et al., 2017; Young et al., 2019). Several studies investigated bulk isotope ($\delta^{13}C$ and δD) fractionation of methane oxidation by lab-cultured aerobic methanotrophic bacteria (Coleman et al., 1981; Templeton et al., 2006), as well as in marine and fresh waters (Kawagucci et al., 2021; Thottathil et al., 2022). Technological advances in the measurement of doubly substituted methane isotopologues ($^{13}CH_3D$ and $^{12}CH_2D_2$, a.k.a. clumped isotopologues) have allowed for development of a novel tool for tracking the formation and consumption of methane gas (Stolper et al., 2014; Wang et al., 2015; Young et al., 2017). At thermodynamic equilibrium, the distribution of $^{13}CH_3D$ and $^{12}CH_2D_2$ within a population of methane molecules correlates with temperature (Cao and Liu, 2012; Liu and Liu, 2016; Eldridge et al., 2019). Therefore, at equilibrium, methane clumped isotope values can be applied as thermometers for tracking the formation temperature (Stolper et al., 2014; Young et al., 2017; Thiagarajan et al., 2020). In contrast, microbial methane often show clumped isotope values that depart from equilibrium, whereas methane synthesized abiotically exhibits signals both at and departed from equilibrium (Stolper et al., 2015; Wang et al., 2015; Douglas et al., 2016; Young et al., 2017; Gruen et al., 2018; Giunta et al., 2019; Gonzalez et al., 2019; Taenzer et al., 2020; Labidi et al., 2020; Etiope and Oze, 2022). These disequilibrium values, combined with bulk isotope signatures, allow us to distinguish methane gases from different sources. However, one of the major problems hindering the application of methane clumped isotope values in natural systems is that the original clumped isotope compositions of a given methane source are susceptible to alteration by microbial methane oxidation, both aerobic (AeOM) and anaerobic (AOM) (Haghnegahdar et al., 2017; Ash et al., 2019; Ono et al., 2021; Giunta et al., 2022).

Prior studies suggest AOM drives methane clumped isotope signatures towards equilibrium at low reaction rates (Ash et al., 2019; Giunta et al., 2019; Ono et al., 2021; Zhang et al., 2021; Liu et al., 2023). In contrast, AeOM generates clumped isotope signatures well off the equilibrium array, and distinct from AOM (Wang et al., 2016; Krause et al., 2022; Giunta et al., 2022). However, the major controls on AeOM methane clumping remain poorly understood. The two experimental studies on AeOM clumped isotope fractionation, while foundational in providing the first one (Wang et al., 2016) and two (Krause et al., 2022) dimensional clumped isotope measurements, do not address the influence of growth rate or enzyme-specific isotope fractionation on methane clumped isotope compositions. The core metabolic processes of AeOM are well understood, and microbial strains such as *Methylococcus capsulatus* strain Bath (referred to hereafter as *M. capsulatus*) are well-characterized both genetically and physiologically (Hanson and Hanson, 1996). Together these make *M. capsulatus* a good target for the study of bulk and clumped isotope fractionation during AeOM across a range of environmental parameters.

Several environmental and physiological parameters can potentially influence the observed clumped isotope signatures of AeOM. Reaction rate can significantly alter the expressed isotope effects during AOM (Ono et al., 2021; Liu et al., 2023), and other isotope fractionation processes (Laws et al., 1995; Leavitt et al., 2013). We therefore predict rate has an impact on the isotope fractionation of AeOM as well. In addition, metal availability, in particular copper (Cu), controls the microbial expression of two types of methane monooxygenases (MMOs) (Stanley et al., 1983; Prior and Dalton, 1985), each of which catalyzes the first critical step in AeOM. Between the two distinct MMOs, a soluble form that uses a diiron active site (sMMO) and a membrane-bound form with a catalytic copper center (pMMO) (Ross and Rosenzweig, 2017), it remains unknown whether each type has different or similar clumped isotope fractionation.

In this study we investigate the trajectory of methane clumped isotope signatures in response to (i) microbial growth and oxidation rates, and (ii) the expression of MMOs controlled by copper concentrations. We evaluate our experimental findings with potential hydrogen re-equilibration between water and methane, and construct a cellular fractionation model that seeks to capture the effects of transport limitation and the closed-system dynamics of the experiments. We then discuss the implications of the experimental isotope fractionation on methane in natural systems.

2. Method

2.1. Microbial culturing

All experiments in this study were performed with *Methylococcus capsulatus* (Bath) acquired from ATCC (ATCC 33009). *M. capsulatus* is an obligate aerobic methanotroph, representative of the wider diversity of aerobic methanotrophic bacteria (Bowman, 2014) that utilize methane for both carbon and energy (Hanson and Hanson, 1996). We performed two types of batch experiments to test the effect of either the two different MMOs (controlled by copper concentration) or the growth rate (controlled by growth temperature) on clumped isotope fractionations. Axenic cultures of *Methylococcus capsulatus* were grown in nitrate mineral salts (NMS) media following established methods (Wang et al., 2016; Welander and Summons, 2012). Briefly, 30 mL NMS medium was dispensed into 160-mL serum bottles, sealed with ambient air at atmospheric pressure and temperature, then injected with 20 mL of filter-sterilized ultra high purity methane (UHP, AirGas, ME). Each serum bottle was inoculated with 1 mL of starter culture at optical densities of ~0.7 (OD_{600}). For the differential temperature experiments, cultures were incubated at 21, 27, or 37 °C in NMS media supplemented with 5 μM $CuSO_4$. For the copper concentration experiments, we used basal NMS medium with starting $CuSO_4$ concentrations at 0 and 50 μM in addition to the 5 μM used in the differential temperature experiments, with all incubations conducted at 37 °C. To test the possibility of hydrogen exchange between methane and medium water, two sets of incubations were done with NMS media made from deuterium enriched (D-spiked) water at nominally +1500 and +3000 ‰ δD under 37 °C and with 5 μM $CuSO_4$ added. For simplicity, the differential temperature experiments are referred to as "37 °C", "27 °C" and "21 °C" experiments, while the differential copper experiments are referred to as "no-Cu" (0 μM) and "high-Cu" (50 μM), respectively. To ensure the exchange of headspace methane with the medium liquid, bottles were shaken at 200 rotations per minute (RPM) in temperature controlled rotary shakers (Innova42, Eppendorf).

A minimum of four time points were sampled from each experiment, with five replicates per time point. The time points for sampling were determined based on the amount of residual methane in the headspace. We selected the time points so that the residual methane decrease by 10%–20% between the two adjacent time points. Typically a minimum of 60 to 80 μmol of methane is targeted for isotopic measurements. Later timepoints have less, but still measurable methane with the cost of lower analytical precision. In addition, one negative control bottle (medium without inoculum) was incubated for each temperature or copper series. From the five replicate bottles, two were designated for monitoring growth (OD_{600}), and the other three for methane sampling at the time of sacrifice. To minimize the chance of methane leakage, the septa of the three methane sample bottles were only punctured to add the methane, the cells, and to measure residual methane at the time

of sacrifice. Microbial growth was quantified by changes in OD_{600} over time. The growth rates and cell doubling times were calculated based on the optical density in the exponential growth phase, following the equations in Brock et al. (2003):

$$\text{Doubling time} = \frac{0.693}{s} \quad (1)$$

where s is the slope of a linear function from the plot of ln(OD) over time during the exponential phase (Figure S1). The errors in doubling time were propagated from the errors of the linear regressions. At each time point of sampling, all five replicates were sampled for residual methane amount by gas chromatography (GC). The five biological replicates were then terminated by the addition of 1 mL 1M HCl to the 30-mL media, and stored inverted at 4 °C until methane extraction. Copper concentrations were measured on the two monitor bottles at the end of growth experiments. Following GC measurements, the media in the monitor bottles were centrifuged without acidification, filtered, then prepared for ICP-OES (see below).

2.2. Analytical techniques

2.2.1. Methane concentration

Methane concentrations in the headspace were monitored by gas chromatography fitted with a flame ionization detector (GC-FID, SRI 8610C) with Grade 5.0 helium (UHP, AirGas). The GC is equipped with a 6' x 1/8" column filled with HayeSep D polymer. During the measurement, the column temperature was held at 120 °C, and the retention time of methane was consistently ~1 min. Methane peaks were integrated with the PeakSimple software. A daily calibration with 1% (v/v) methane/helium standard (AirGas) was done to ensure the analytical linearity of the instrument prior to the measurements. Headspace gas was sampled from each bottle (40 μL) using a calibrated gas-tight syringe with a valve (100-μL; Hamilton Company) for the quantification of methane concentrations. The results were then converted to total headspace methane in each bottle. The uncertainty of each sample was propagated from the error in the GC calibration. Dissolved methane in the media was calculated following Yamamoto et al. (1976).

2.2.2. Dissolved copper concentration

Dissolved copper concentrations in the medium were measured using an inductively coupled plasma - optical emission spectrometer (ICP-OES; axial-view Spectro ARCOS), and calculated from the variance-weighted average of the two emission lines, 324 and 327 nm (Landis et al., 2021). The standards were matrix-matched to the samples, with an independent calibration verification standard showing residual standard deviation typically smaller than 2%. The standards were measured every five samples to correct for the time-dependent drift. The instrument detection limit (IDL) was calculated as 3x standard deviation of blank measurements (in ng/mL). For copper, the IDL is 3.9 ng/mL (0.0614 μM), which was sufficient for monitoring the change of copper concentrations during the experiment. Each sample was measured twice and the average values of the two measurements were taken as the final results, as shown in Table S1.

2.2.3. Isotopic measurements

Prior to isotopic measurements, methane was purified from other headspace gases on a vacuum line. The procedure was modified based on the method described in Young et al. (2017) and Taenzer et al. (2020). The gas was introduced from serum bottles into the vacuum line through an SGE on/off valve (SMOV) with a needle attached to it. The gas was then equilibrated between the bottle and the vacuum line for 5 min to avoid fractionation, after which the SGE valve was closed. Water vapor and carbon dioxide were trapped in a U-trap by pure liquid nitrogen (LN_2) at −185 °C. Methane was trapped in a U-trap containing silica gel at LN_2 temperature, followed by entrainment in 5.5 grade He and transport to a GC (SRI GC-TCD 8610). Purification of CH_4 from non-condensible atmospheric gases (Ar, O_2, N_2) and higher-order organics was accomplished using two in-series packed GC columns. One is a 3-meter 1/8 inch OD stainless steel (SS) filled with 5 A molecular sieve and the other is a 2-meter 1/8 inch OD SS column with HayeSep D polymer. After GC purification, methane gas was trapped in a second U-trap filled with silica gel at LN_2 temperature, followed by pumping away the He carrier gas. The purified methane gas was then collected in a sample vial with silica gel at LN_2 temperature and transferred via a small-volume cold finger, also containing silica gel, to the mass spectrometer for isotopic measurements.

The isotopic compositions of headspace methane were measured on the prototype high-resolution, double-focusing mass spectrometer, Panorama (Nu Instruments, AMETEK Inc.) at UCLA. To resolve two mass-18 isotopologues of methane ($^{13}CH_3D$ and $^{12}CH_2D_2$), as well as interfering species, the instrument was run at a mass resolving power of ~40,000 or above (Young et al., 2016). We utilized a combination of Faraday collectors with 10^{11} Ω resistors and a single channel of ion counting for these measurements. Isotopic ratios of the samples were measured relative to a reference methane gas under two magnet current settings. The first setting placed $^{13}CH_3D^+$ in the axial electron multiplier collector. $^{13}CH_4{}^+/^{12}CH_4{}^+$ and $^{13}CH_3D^+/^{12}CH_4{}^+$ ratios were obtained after 6 to 20 blocks of twenty 30-s integration cycles. The second setting placed $^{12}CH_2D_2{}^+$ in the axial collector where $^{12}CH_3D^+/^{12}CH_4{}^+$ and $^{12}CH_2D_2{}^+/^{12}CH_4{}^+$ ratios were obtained after 16 to 40 blocks of twenty 30 s integration cycles (Young et al., 2017). The number of blocks used for each measurement depended on the size of the methane sample, with a maximum number of 40. Fewer blocks of measurements generally resulted in larger internal 1σ uncertainties. The internal 1σ uncertainties (propagation of standard errors in the means for all blocks) of the samples are typically better than ±0.01 ‰ for $\delta^{13}C$, ±0.09 ‰ for δD, ±0.3 ‰ for $\Delta^{13}CH_3D$, and ±0.8 ‰ for $\Delta^{12}CH_2D_2$, with few exceptions (Table 1).

Isotopic compositions of medium water were measured in the Stable Isotope Laboratory at Dartmouth College following the procedures described previously by Kopec et al. (2019) using an H-Device coupled to a Thermo Delta Plus XL dual-inlet isotope ratio mass spectrometer (IRMS). Measured values were converted to the water isotope equivalent by calibration with known standards. Deuterium-spiked water samples outside the range of working standards were diluted with water of known isotopic compositions before measurement following the procedure in Taenzer et al. (2020). Uncertainties in mass spectrometry measurements and dilutions were propagated into the result of each measurement. The average values and the standard deviations among the four biological replicates in each set of experiment were taken as the final results. Isotope ratios are reported as δD in ‰ relative to VSMOW, as shown in Table S2.

2.3. Isotope notations and calculations

2.3.1. Isotope notations

Bulk isotope ratios for methane in this study are reported using standard delta-notation (in ‰ relative to international standards):

$$\delta^{13}C = 10^3\left(\frac{(^{13}C/^{12}C)_{sample}}{(^{13}C/^{12}C)_{VPDB}} - 1\right) \quad (2)$$

$$\delta D = 10^3\left(\frac{(D/H)_{sample}}{(D/H)_{VSMOW}} - 1\right) \quad (3)$$

where VPDB refers to the Vienna Pee Dee Belemnite and VSMOW refers to Vienna Standard Mean Oceanic Water.

Clumped isotope compositions are expressed using the capital delta notation in ‰ relative to the corresponding stochastic distribution for the sample in which isotopes are randomly distributed among the CH_4 isotopologues (Wang et al., 2004):

$$\Delta^{13}CH_3D = 10^3\left(\frac{([^{13}CH_3D]/[^{12}CH_4])_{sample}}{([^{13}CH_3D]/[^{12}CH_4])_{stochastic}} - 1\right) \quad (4)$$

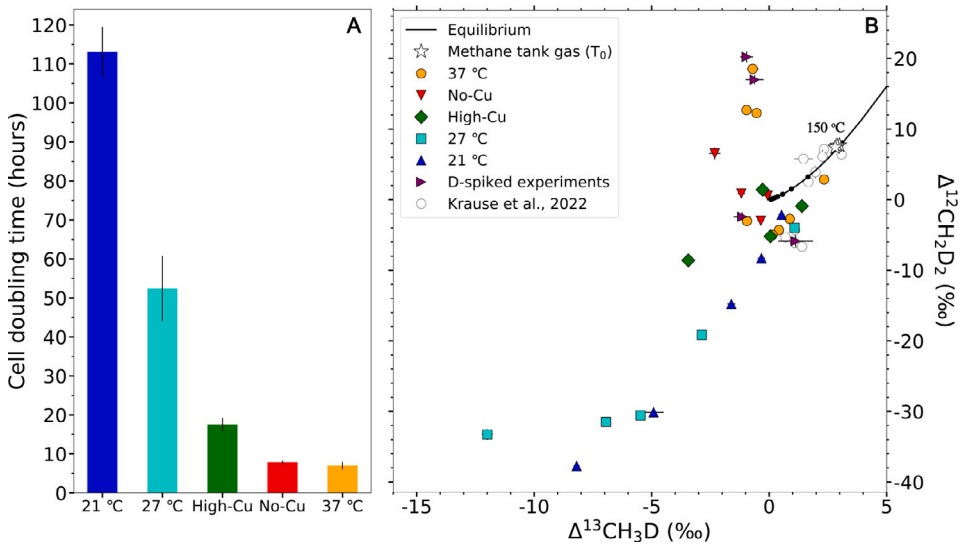

Fig. 1. Cell doubling time of experimental culture (panel A) and clumped isotope signatures of headspace methane in $\Delta^{12}CH_2D_2$ vs. $\Delta^{13}CH_3D$ space (panel B). In panel A, longer cell doubling time represents slower growth rate. In panel B, the growth conditions are shown as growth temperature or total copper concentration in the legend. Experiments under different growth temperature are conducted with 5 μM copper-supplemented media. Experiments with different copper concentrations are under 37 °C. High- and no-Cu correspond to 50 and 0 μM Cu, respectively. The equilibrium curve in panel B is based on the equilibrium clumped isotope values in Young et al. (2017). The temperature increment between two adjacent points is 150 °C. The clumped isotope data from Krause et al. (2022) are shown for comparison as hollow circles.

$$\Delta^{12}CH_2D_2 = 10^3\left(\frac{([^{12}CH_2D_2]/[^{12}CH_4])_{sample}}{([^{12}CH_2D_2]/[^{12}CH_4])_{stochastic}} - 1\right). \quad (5)$$

Here the bracketed values represent the concentrations of methane isotopologues. Equilibrium values of $\Delta^{13}CH_3D$ and $\Delta^{12}CH_2D_2$ used in this study are derived from the equilibrium constants in Young et al. (2017).

2.3.2. Calculations of apparent fractionation and clumped isotopologue factors

Bulk isotope fractionation in a closed system is expected to follow the Rayleigh equation where the reactants (in this case CH_4 gas) are well mixed throughout the process. Therefore calculating net fractionation factors follows the specific forms used here for methane $^{13}C/^{12}C$ and D/H after (Mariotti et al., 1981):

$$\ln\frac{\delta^{13}C + 1000}{\delta^{13}C_{init} + 1000} = ({}^{13}\alpha - 1)\ln f \quad (6)$$

and

$$\ln\frac{\delta D + 1000}{\delta D_{init} + 1000} = ({}^{D}\alpha - 1)\ln f \quad (7)$$

where the $^{13}\alpha$ and $^{D}\alpha$ are the net fractionation factors for $^{13}C/^{12}C$ and D/H, respectively. The $\delta^{13}C$ and δD are the bulk isotope values of residual methane (in ‰) at the time of sampling, and the $\delta^{13}C_{init}$ and δD_{init} are the values of methane (in ‰) at the start of the experiment. Here f is taken to be the fraction of methane remaining relative to the initial headspace methane (Fig. 2). The net fractionation factors for the doubly-substituted isotopologues can be expressed similarly as:

$$\ln\frac{\delta^{13}CH_3D + 1000}{\delta^{13}CH_3D_{init} + 1000} = ({}^{13CD}\alpha - 1)\ln f \quad (8)$$

and

$$\ln\frac{\delta^{12}CH_2D_2 + 1000}{\delta^{12}CH_2D_{2init} + 1000} = ({}^{DD}\alpha - 1)\ln f \quad (9)$$

where $^{13CD}\alpha$ and $^{DD}\alpha$ are the net fractionation factors for $^{13}CH_3D$ and $^{12}CH_2D_2$, respectively, following prior studies (Wang et al., 2016; Liu et al., 2023).

These equations predict that if the isotope fractionations are Rayleigh-like, the relationship between observed fractionations (left hand sides of Eqs. (6) to (9)) and corresponding $\ln f$ values is linear with slopes of $(\alpha - 1)$. The net fractionation factors for our experiments, α, are therefore calculated from slopes defined by plots of observed fractionations and $\ln f$ values as determined by least-squares (York et al., 2004). The derived fractionation factors and 1σ uncertainties for the experiments at 37 °C, 27 °C and 21 °C are shown in Table 2. An important feature of both the 37 °C and 27 °C experiments is the apparent change in net fractionation factors occurring at low f (high $-\ln f$) values (Fig. 3), where the linearity of the regression is noticeably degraded if all data points are fit with a single line (Figs. 3A, 3B, 3E, 3F). To address these changes, two separate sets of fractionation factors are calculated for the 37 °C and 27 °C experiments, respectively. The first set is calculated for the first five points in the 37 °C experiment, with f between 0.668 and 1.000. The second set is calculated for the last four points in the same experiment, with f ranging from 0.227 to 0.556 (Fig. 3). For the 27 °C experiment, the first set of fractionation factors is calculated using the first four points with f values 0.374 and 1.000. Then the fourth data point (f = 0.374) and the last two points with lower f values are used for calculating the second set of fractionation factors (Figs. 3A, 3B, 3E and 3F). We used the two-tailed t-test to examine if the two slopes in each experiment were significantly different. For comparison, we also modeled the results using the fractionation factors without the divisions (Figure S2), where we used the equations described in Wang et al. (2016) and Liu et al. (2023) to calculate the oxidation trajectory of a closed-system Rayleigh process as a function of f:

$$\Delta^{13}CH_3D(f) = \Delta^{13}CH_3D_{init} + 10^3({}^{13CD}\alpha - {}^{13}\alpha - {}^{D}\alpha + 1)\ln f \quad (10)$$

and

$$\Delta^{12}CH_2D_2(f) = \Delta^{12}CH_2D_{2init} + 10^3({}^{DD}\alpha - 2({}^{D}\alpha) + 1)\ln f. \quad (11)$$

$\Delta^{13}CH_3D_{init}$ and $\Delta^{12}CH_2D_{2init}$ are the initial clumped isotope signatures of methane, and $\Delta^{13}CH_3D(f)$ and $\Delta^{12}CH_2D_2(f)$ are the clumped isotope signatures of methane at a specified value for f.

We also considered clumped isotopologue factors (γ), which (Wang et al., 2016) utilize to describe deviations from the rule of the geometric mean:

$${}^{13CD}\alpha = {}^{13CD}\gamma\,{}^{13}\alpha\,{}^{D}\alpha \quad (12)$$

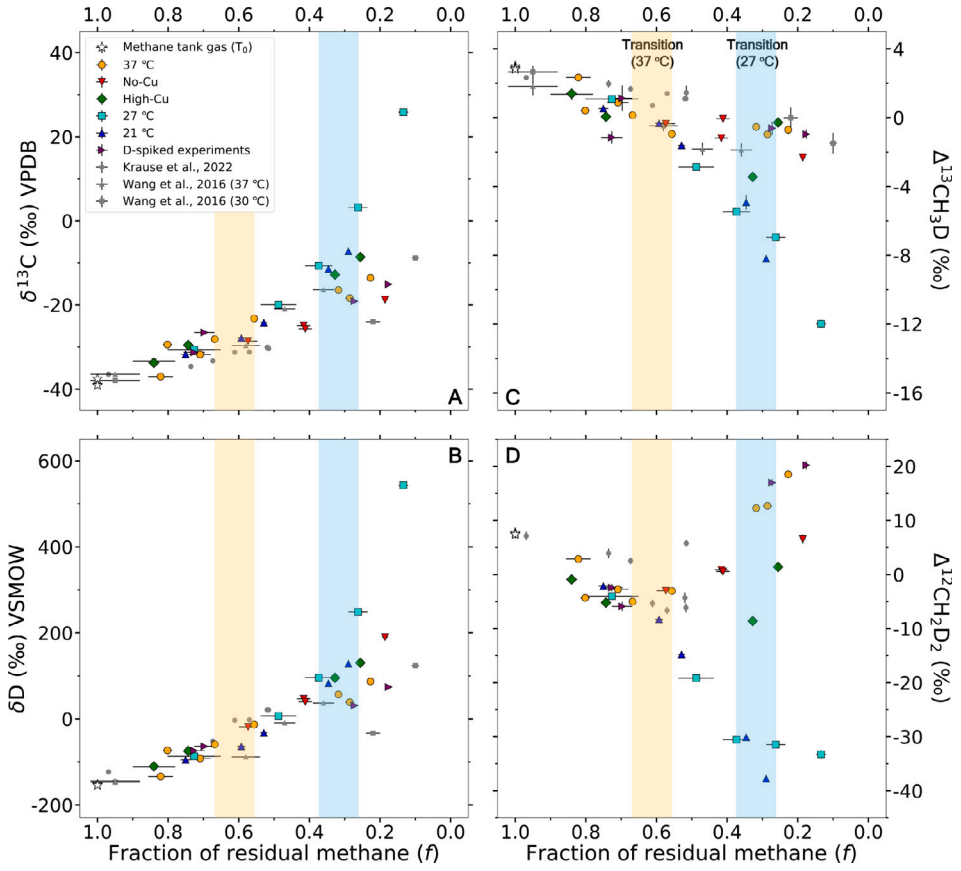

Fig. 2. Variations of isotopic compositions with the fraction of headspace methane remaining after oxidation (f): (A) $\delta^{13}C$; (B) δD; (C) $\Delta^{13}CH_3D$; (D) $\Delta^{12}CH_2D_2$. In each panel, lower f values (the right side) represent more methane consumption. The light yellow and the blue bars show the range of f values where the isotope signatures start to deviate from the Rayleigh fractionation in 37 °C and 27 °C experiments. Data from previous studies (Wang et al., 2016; Krause et al., 2022) are included as the gray data points in the figure.

and

$$^{DD}\alpha = {}^{DD}\gamma(^{D}\alpha)^2. \quad (13)$$

When γ is equal to unity, the clumped isotopologue frationation factors are the product of the fractionation factors for the heavy isotopes they contain (e.g. $^{13}CD^{\alpha} = {}^{13}\alpha\, D^{\alpha}$), following the rule of the geometric mean (Bigeleisen, 1955). In this scenario, there is no energy difference between the addition of a heavy isotope to a singly-substituted and non-substituted isotopologues (e.g. $^{12}CH_3$ + D and $^{12}CH_2D$ + D).

3. Results

Microbial growth rates presented across all experimental treatments in Fig. 1A are calculated from OD_{600} measurements over time as shown in Figure S1. Doubling times vary over an order of magnitude, from 7 to 113 h. The longest doubling time (slowest growth rate) corresponds to the lowest growth temperature of 21 °C while the shortest doubling time (fastest growth rate) is obtained from the 37 °C experiments, consistent with the optimal conditions for this strain Welander and Summons (2012). Maximum OD_{600} values from temperature experiments range from ~0.32 at 21 °C to ~0.67 at 37 °C, respectively (Figure S1). The growth profiles of the D-spiked experiments are similar to the unspiked 37 °C experiments.

Total headspace methane quantities are plotted in Figure S1. The average amounts of methane consumed differed across experimental conditions. In 37 °C, 27 °C and no-Cu experiments, the average methane amount decreases from around 600 μmol to less than 100 μmol. On the other hand, high-Cu and 21 °C experiments have less total methane consumption, from around 600 μmol to around 200 μmol. The amount of methane in each serum bottle is also expressed as the fraction of residual methane (f) relative to the initial headspace methane, as shown in Table 1 and Fig. 2. Dissolved methane only composes ~ 0.1% of headspace methane in each sample, so it is neglected in the calculation of total methane. The lowest f value is 0.134, corresponding to 85.1 μmol of headspace methane, which is approaching the minimum methane amount required for purification and mass spectrometry. Total methane oxidation rate increases from 8.89 to 30.88 μmol/h and 1.94 to 3.79 μmol/h in 37 °C and 27 °C experiments, respectively (Figure S1). In contrast, oxidation rate in the 21 °C experiment stays constant at 0.96 μmol/h (Figure S1).

Dissolved copper concentrations ($[Cu^{2+}]_{aq}$) in the media range from 0.043 ± 0.026 to 0.864 ± 0.029 μM in 5 μM Cu-supplemented experiment, with lower $[Cu^{2+}]_{aq}$ towards the end of the experiment. The $[Cu^{2+}]_{aq}$ ranges from 7.54 ± 0.06 to 9.19 ± 0.06 μM in 50 μM (high) Cu-supplemented experiment, with no significant decrease towards the end of the experiment. The $[Cu^{2+}]_{aq}$ of the no-Cu experiment is around zero throughout the experiment, considering 1σ error (Table S1, Figure S3).

The measured $\delta^{13}C$ of all samples are between −39.10 ± 0.01 to 25.84 ± 0.02 ‰ (1σ, same thereafter) VPDB and δD are in the range of −153.97 ± 0.02 to 543.32 ± 0.09 ‰ VSMOW (Table 1, Fig. 2A, 2B). Consistent enrichment of heavier isotopes (^{13}C and D) in residual methane is observed in all experiments. The average $\Delta^{13}CH_3D$ and $\Delta^{12}CH_2D_2$ values for the methane tank gas are 2.90 ± 0.09 ‰ and 7.6 ± 0.2 ‰ (Table 1, Fig. 1B), which are close to the equilibrium values at 165 °C. The measured $\Delta^{13}CH_3D$ values from all experiments range from −11.99 ± 0.23 ‰ to 2.99 ± 0.19 ‰ while $\Delta^{12}CH_2D_2$ range from −37.7 ± 0.6 to 20.2 ± 0.8 ‰ (Table 1, Fig. 1B). $\Delta^{13}CH_3D$ values consistently decrease with more methane consumption in the majority

Table 1
Isotopic data of headspace methane in aerobic methane oxidation by *Methylococcus capsulatus* (Bath). Experimental conditions are represented as either growth temperature or copper concentration in the column "Experimental groups". The differential temperature experiments are conducted with 5 μM Cu in the media, and the differential copper experiments are conducted under 37 °C. The 1σ errors are listed following each measured variables.

Experimental groups	Sample name[a]	f	1σ	δ^{13}C (‰)	1σ	δD (‰)	1σ	$\Delta^{13}CH_3D$ (‰)	1σ	$\Delta^{12}CH_2D_2$ (‰)	1σ
Control[b]	27 °C 5 μM Ctrl	1.000	N/A[c]	−39.006	0.011	−153.655	0.020	2.992	0.193	7.715	0.643
	CH_4 tank gas	1.000	N/A	−37.544	0.006	−152.678	0.019	2.889	0.158	7.679	0.672
	37 °C 5 μM Ctrl	1.000	N/A	−39.095	0.007	−153.968	0.024	2.809	0.197	7.417	0.708
37 °C[d]	37 °C 5 μM T1 C3 exp2	0.821	0.035	−37.023	0.008	−133.900	0.023	2.336	0.183	2.858	0.649
	37 °C 5 μM T1 C4 exp1	0.802	0.013	−29.418	0.014	−73.200	0.020	0.414	0.165	−4.307	0.567
	37 °C 5 μM T2 C1 exp2	0.709	0.030	−31.781	0.008	−92.041	0.024	0.877	0.165	−2.734	0.635
	37 °C 5 μM T1 C2 exp1	0.668	0.011	−28.143	0.003	−59.417	0.017	0.141	0.197	−4.994	0.576
	37 °C 5 μM T2 C2 exp1	0.556	0.009	−23.215	0.003	−13.248	0.023	−0.945	0.127	−3.029	0.650
	37 °C 5 μM T3 C3 exp1	0.318	0.005	−16.442	0.006	56.858	0.024	−0.537	0.170	12.270	0.596
	37 °C 5 μM T3 C3 exp2	0.286	0.012	−18.377	0.005	39.009	0.029	−0.964	0.161	12.692	0.656
	37 °C 5 μM T4 C4 exp1	0.227	0.004	−13.548	0.007	87.230	0.032	−0.702	0.242	18.526	0.711
No-Cu	37 °C 0 μM T2 C2	0.574	0.026	−28.586	0.007	−18.548	0.019	−0.356	0.141	−2.989	0.510
	37 °C 0 μM T3 C3	0.416	0.019	−24.897	0.004	46.795	0.027	−1.185	0.152	0.883	0.584
	37 °C 0 μM T3 C1	0.412	0.019	−25.688	0.006	39.623	0.017	−0.065	0.157	0.567	0.441
	37 °C 0 μM T4 C1	0.186	0.009	−18.744	0.009	190.055	0.053	−2.315	0.241	6.550	0.856
High-Cu	37 °C 50 μM T2 C2	0.840	0.016	−33.747	0.007	−110.412	0.026	1.394	0.144	−0.905	0.654
	37 °C 50 μM T3 C2	0.743	0.014	−29.542	0.008	−74.580	0.021	0.053	0.146	−5.194	0.588
	37 °C 50 μM T4 C1	0.328	0.006	−12.784	0.008	95.454	0.026	−3.440	0.158	−8.596	0.531
	37 °C 50 μM T4 C2	0.256	0.005	−8.596	0.005	130.494	0.028	−0.281	0.149	1.413	0.524
27 °C	27 °C 5 μM T2 C2	0.726	0.075	−30.591	0.003	−87.010	0.020	1.080	0.120	−3.990	0.500
	27 °C 5 μM T3 C3	0.488	0.051	−19.955	0.005	6.987	0.020	−2.865	0.148	−19.150	0.502
	27 °C 5 μM T4 C1	0.374	0.039	−10.695	0.005	96.042	0.027	−5.473	0.138	−30.568	0.582
	27 °C 5 μM T3 C4	0.262	0.027	3.203	0.003	249.234	0.044	−6.943	0.107	−31.479	0.619
	27 °C 5 μM T4 C2	0.134	0.014	25.836	0.017	543.317	0.085	−11.993	0.232	−33.258	0.764
21 °C	21 °C 5 μM T2 C2	0.751	0.014	−31.719	0.009	−95.285	0.019	0.529	0.129	−2.144	0.570
	21 °C 5 μM T3 C2	0.593	0.011	−27.833	0.003	−63.890	0.015	−0.329	0.158	−8.289	0.444
	21 °C 5 μM T3 C4	0.529	0.010	−24.208	0.005	−32.559	0.023	−1.610	0.167	−14.776	0.630
	21 °C 5 μM T4 C4	0.346	0.006	−11.449	0.008	82.803	0.022	−4.918	0.429	−30.120	0.588
	21 °C 5 μM T4 C3	0.290	0.005	−7.227	0.004	128.196	0.032	−8.194	0.132	−37.740	0.587
D-spiked[e]	1433 T1 C1	0.726	0.030	−31.253	0.052	−74.028	0.019	−1.148	0.361	−2.419	0.653
	1433 T2 C3	0.273	0.011	−19.097	0.042	31.170	0.031	−0.616	0.383	16.983	0.645
	3008 T1 C2	0.697	0.029	−26.547	0.283	−63.940	0.030	1.127	0.740	−5.887	0.837
	3008 T2 C2	0.176	0.007	−15.083	0.017	74.137	0.026	−0.960	0.273	20.224	0.752

[a] The sample names consist the growth temperatures (37, 27, 21 °C), copper concentrations (0, 5, 50 μM), time of sacrifice (T1–T4) and the number of replicate (C1–C4).
[b] The control group includes two headspace methane samples from the control bottles (27 °C 5 μM Ctrl and 37 °C 5 μM Ctrl), and one methane sample from the tank gas (CH_4 tank gas). These samples represent the initial headspace methane.
[c] N/A, not applicable. The fraction of residual methane is set as 1.000 without 1σ error, since no methane was consumed at the start.
[d] 37 °C is a compilation of two sets of experiments of the same growth condition, without significant difference in microbial growth between them. They are denoted as exp1 and exp2 in Sample names.
[e] D-enriched ('spiked') experiments contain water with two highly enriched δD values of +1433 and +3008 ‰, in replicate. The δD values of water are shown in the sample names.

of the experiments. However, the 37 °C and high-Cu experiments present insignificant and increasing trends after half of the initial methane is consumed ($f < 0.5$), respectively (Fig. 2C). More prominent decrease of $\Delta^{13}CH_3D$ values are observed at lower growth temperatures. Similarly, $\Delta^{12}CH_2D_2$ values decrease with methane consumption at lower growth temperatures (21 and 27 °C). In contrast, in the experiments at 37 °C, $\Delta^{12}CH_2D_2$ values decrease slightly at high methane concentrations ($f > 0.5$) and then increase at low methane concentrations ($f < 0.5$), as shown in Fig. 2D. The measured δD for the media of the D-spiked experiments ranges from 1419 ± 3 to 1440 ± 3 ‰, and from 3003 ± 6 to 3017 ± 7 ‰ in two sets of D-spiked experiments, respectively (Table S2). The average values across biological replicates are 1433 ± 10 ‰ (1 standard deviation) and 3008 ± 6 ‰. The isotope signatures of the two D-spiked experiments follow the same pattern as the non-spiked experiment at 37 °C, so they are discussed together as one set of experiment in the following sections.

Net fractionation factors across all experiments range from 0.9649 ± 0.0049 to 0.9911 ± 0.0005 for $^{13}\alpha$ (Fig. 3A, 3C), from 0.6683 ± 0.0466 to 0.8892 ± 0.0028 for D^{α} (Fig. 3B, 3D), from 0.6396 ± 0.0507 to 0.8775 ± 0.0031 for $13CD^{\alpha}$ (Fig. 3E, 3G), and from 0.3392 ± 0.0929 to 0.7542 ± 0.0064 for DD^{α} (Fig. 3F, 3H). Two-tailed t-tests show that D^{α}, $13CD^{\alpha}$ and DD^{α} (i.e. the slopes of the regression lines) for $f \geq 0.668$ and $f \leq 0.556$ in the 37 °C experiments are significantly different ($p < 0.005$). Similarly, the three fractionation factors of low-Cu ($f \leq 0.574$) are significantly different from those of the 37 °C ($f \geq 0.668$) experiment ($p<0.01$ for $13CD^{\alpha}$ and $p<0.02$ for D^{α} and DD^{α}). These three fractionation factors are not significantly different between the high-Cu ($f \geq 0.743$) and the 37 °C ($f \leq 0.556$) experiments if the confidence interval is 95% but is significantly different if the confidence interval is 90% for two-tailed test ($p<0.1$). In contrast, $^{13}\alpha$ is only significantly different between high-Cu ($f \geq 0.743$) and the 37 °C ($f \leq 0.556$) experiment ($p < 0.1$). This indicates less variability of carbon isotope fractionation with progressive methane consumption in the experiments. On the contrary, none of the four fractionation factors is significantly different between $f \geq 0.374$ and $f \leq 0.374$ in the 27 °C experiments.

4. Discussion

4.1. Net isotope fractionation factors

We performed separate linear regressions for the data with high and low f in the 37 °C for two major reasons: first, the t-test indicates that the two fractionation factors are significantly different. Second, the fit of experimental data is very poor using a single set of fractionation factors (Figure S2). For the 27 °C experiment, although t-test shows no significant difference between the fractionation factors at high and low f, the fit for the experimental clumped isotope data is compromised by adding the last two points into the regression (Figure S2). Therefore, separating the data into two groups and calculating two sets of fractionation factors are better for describing and modeling the system.

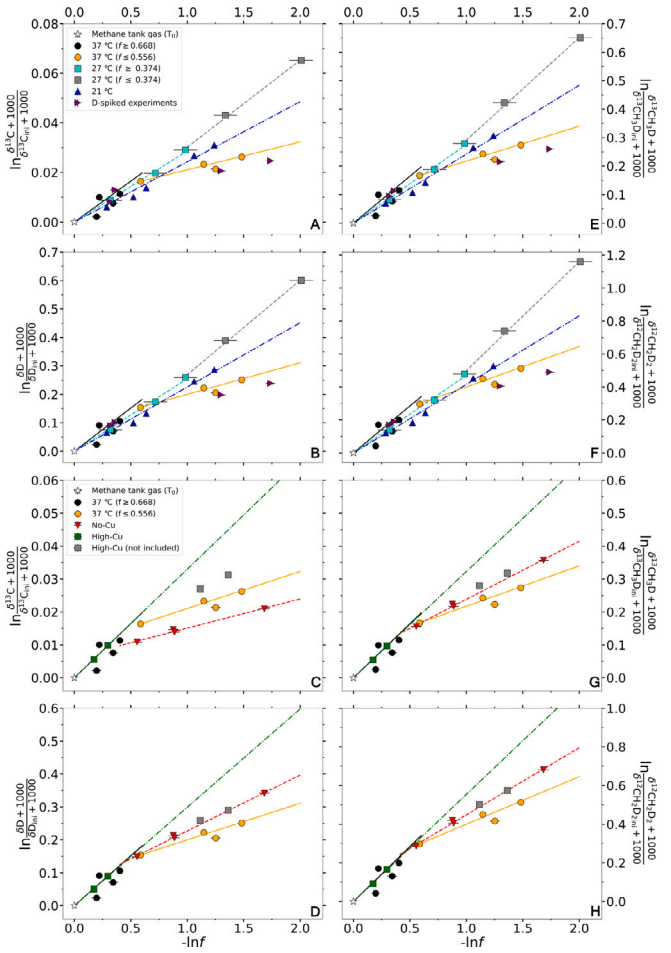

Fig. 3. Linear regressions for calculating net fractionation factors for different temperatures, water spikes and copper concentrations. The slopes of the regression lines are 1-α, where α is the net fractionation factor of the isotope or isotopologue assuming a Rayleigh fractionation process (values are shown in Table 2). Panels A to D show the $^{13}\alpha$ and D$^{\alpha}$ across temperatures and copper concentrations; panels E and H show the 13CD$^{\alpha}$ and DD$^{\alpha}$ for different temperatures and copper concentrations. The right side of each panel represents lower f values. Within the 37 °C experiment (orange and black circles in panels A, B, E, F), the net fractionation of $f \leq 0.556$ (orange circles) is significantly different from $f \geq 0.668$ (black circles). In the 27 °C experiment (gray and cyan squares in panels A, B, E, F), the net fractionation is also different between $f \leq 0.374$ (gray squares) and $f \geq 0.374$ (cyan squares). The isotope signatures of deuterium-spiked experiments (purple triangles in panels A, B, E, F) are not significantly different from non-spiked experiments at the same temperature, regardless of the spike. Two data points (gray rectangles in panels C, D, G, H) in the high-Cu experiment are not included in the regression, as they deviate from the Rayleigh curve determined by the first three points, and they are not enough to do a separate linear regression. Regardless of copper concentrations, deviation from Rayleigh fractionation still occurs at low f (panels C, D, G, H).

The net fractionation during the early stages of all experiments are comparable (Table 2), as reflected by the similarities in the trends of isotope signatures in the 37 °C ($f \geq 0.668$), 27 °C ($f \geq 0.374$), 21 °C and high-Cu ($f \geq 0.743$) experiments (Fig. 1B; Fig. 2). During the early stages of all experiments, the net fractionation factors also scale inversely with temperatures (Table 2). The net fractionation factors shift towards unity at low methane concentration for the 37 °C experiments (Table 2; Fig. 3) regardless of copper concentrations, indicating less discrimination between heavy to light isotopologues at low f values, as methane was depleted. In contrast, the 27 °C experiment exhibits more net fractionation at low methane concentration (Table 2; Fig. 3A, 3B, 3E, 3F), such that the reaction shows preference for the light isotopes or isotopologues late into the reaction coordinate. The 21 °C experiment shows a consistent net fractionation over the whole experiment (Table 2; Fig. 3A, 3B, 3E, 3F).

The bulk isotope fractionation factors $^{13}\alpha$ and D$^{\alpha}$ broadly agree with the direction and magnitude of those previously reported (Feisthauer et al., 2011; Rasigraf et al., 2012). This said, we observe more D/H fractionation, with the 37 °C ($f \geq 0.668$) and 27 °C ($f \leq 0.374$) experiments yielding D$^{\alpha}$ = 0.6967 ± 0.0101 and 0.6683 ± 0.0466, respectively, whereas the previously estimated D/H fractionation values for MMO range from 0.7685 ± 0.0303 to 0.8900 ± 0.0115 (Feisthauer et al., 2011; Rasigraf et al., 2012). The range of isotope fractionation factors in the 37 °C experiment encompass the factors from Wang et al. (2016) at the same temperature (Table 2). The fractionation factors in our 21 °C experiment with *M. capsulatus* agree with the values obtained at room temperature (~20 °C) using a different strain, *Methylosinus trichosporium* OB3b (Krause et al., 2022). This is reasonable since both strains possess pMMO and sMMO for methane oxidation. Despite the deviation from purely Rayleigh fractionation, $^{13CD}\gamma$ in all our experiments are close to unity within 1σ error (Table 2), consistent with previous reports (Wang et al., 2016; Krause et al., 2022). On the other hand, $^{DD}\gamma$ shows large differences across the experimental conditions tested, ranging from 0.7595 ± 0.2334 to 0.9745 ± 0.0091. The highest $^{DD}\gamma$ value (0.9745 ± 0.0091), occurring in the 21 °C experiment, is higher than the value from Krause et al. (2022) (0.9013 ± 0.0045) at a similar growth temperature, indicating less deviation from the rule of geometric mean. In contrast, in the 37 °C ($f \geq 0.668$) experiment, the $^{DD}\gamma$ is 0.8877 ± 0.0474, which is closer to the value from Krause et al. (2022), albeit at different temperatures. The 27 °C ($f \leq 0.374$) experiment has the lowest $^{DD}\gamma$ value (0.7595 ± 0.2334), showing the most deviation from the rule of geometric mean.

One prominent feature in our experiments is the change of net isotope fractionation during the progressive oxidation of methane (Fig. 3, Table 2). Similar changes in bulk carbon isotope fractionation are reported by Templeton et al. (2006), and attributed to an increase in the total methane oxidation rate relative to the rate of methane conversion from the gaseous to the dissolved state and diffusion into the cells. In another study, the variation of net carbon isotope fractionation with temperature was attributed to the ratio of adsorption and desorption of methane onto the cell wall and the rate of conversion from methane to methanol (Nihous, 2010). To explore this possibility in our experiments, we investigate three scenarios that could generate the observed changes in apparent fractionation factors within the three differential temperature experiments. These scenarios are (i) differential enzyme isotope effects as a function of dissolved copper, (ii) isotopic re-equilibration between methane and water, and (iii) reservoir effects related to the ratio between the rate of methane transport across the cell membrane and the total methane oxidation rate.

4.1.1. *Enzymatic effect on net fractionation*

It is possible that the changes in the net fractionation factor originate from the switch of methane oxidation pathways. The first step in AeOM (from methane to methanol) is catalyzed by two isoforms of the methane monooxygenase enzyme, the particulate methane monooxygenase (pMMO) and the soluble methane monooxygenase (sMMO) (Sirajuddin and Rosenzweig, 2015; Ross and Rosenzweig, 2017). Key differences between the two enzymes include either a monocopper, dicopper, or zinc/copper active site in pMMO, whereas sMMO possesses only a diiron active site (Sirajuddin and Rosenzweig, 2015). The oxygen activation mechanism by the diiron center of sMMO is well studied (Gassner and Lippard, 1999), while the catalytic mechanism behind pMMO is less well characterized (Koo and Rosenzweig, 2021). The *M. capsulatus* genome encodes both pMMO and sMMO (Ribbons and Michalover, 1970; Colby et al., 1977), and the expression of pMMO versus sMMO proteins is controlled by environmental concentrations of copper. High copper concentrations induce the organism to express pMMO and therefore lead to high pMMO activity, whereas limited or no copper induces cells to express sMMO – this is known as the “copper

Table 2
Experimentally-derived net fractionation factors in this study and published data in Wang et al. (2016) and Krause et al. (2022). The numbers in parentheses represent the range of f for the data used in the calculation.

Experiment	$^{13}\alpha$	1σ	$^{D}\alpha$	1σ	$^{13CD}\alpha$	1σ	$^{13CD}\gamma$	1σ	$^{DD}\alpha$	1σ	$^{DD}\gamma$	1σ
37 °C ($f \geq 0.668$)	0.9671	0.0011	0.6967	0.0101	0.6716	0.0110	0.9968	0.0218	0.4309	0.0193	0.8877	0.0474
37 °C ($f \leq 0.556$)	0.9887	0.0003	0.8892	0.0028	0.8775	0.0031	0.9981	0.0047	0.7542	0.0064	0.9539	0.0101
27 °C ($f \geq 0.374$)	0.9713	0.0024	0.7452	0.0209	0.7249	0.0227	1.0015	0.0422	0.5291	0.0387	0.9528	0.0878
27 °C ($f \leq 0.374$)	0.9649	0.0049	0.6683	0.0466	0.6396	0.0507	0.9919	0.1048	0.3392	0.0929	0.7595	0.2334
21 °C	0.9757	0.0002	0.7742	0.0022	0.7580	0.0024	1.0035	0.0043	0.5841	0.0043	0.9745	0.0091
No-Cu ($f \leq 0.574$)	0.9911	0.0005	0.8304	0.0093	0.8234	0.0097	1.0005	0.0163	0.6526	0.0191	0.9464	0.0349
High-Cu ($f \geq 0.743$)	0.9670	0.0018	0.7012	0.0161	0.6772	0.0175	0.9987	0.0346	0.4459	0.0303	0.9069	0.0744
Krause et al. (20 °C)	0.9848	0.0001	0.7265	0.0010	0.7141	0.0011	0.9981	0.0017	0.4757	0.0023	0.9013	0.0045
Wang et al. (30 °C)	0.9880	0.0003	0.8950	0.0030	0.8847	0.0030	1.0005	0.0003	N/A	N/A	N/A	N/A
Wang et al. (37 °C)	0.9780	0.0010	0.7980	0.0100	0.7804	0.0098	1.0000	0.0007	N/A	N/A	N/A	N/A

switch" (Stanley et al., 1983; Prior and Dalton, 1985; Nielsen et al., 1997; Koo and Rosenzweig, 2021).

In this study, progressive and substantial cellular uptake of dissolved copper occurs during population growth, which is indicated by the significant drop of $[Cu^{2+}]_{aq}$ in the 37 °C experiments with 5 μM initial dissolved copper (Figure S3). It is worth noting that the maximum $[Cu^{2+}]_{aq}$ in both Cu-supplemented experiments are lower than the total Cu added by five to six fold due to the precipitation of copper salts. However, the loss of $[Cu^{2+}]_{aq}$ due to microbial uptake is replenished by the re-dissolution of Cu-bearing precipitates, which is supported by the observation that the $[Cu^{2+}]_{aq}$ remains above 7 μM over the entirety of the high-Cu experiment (Figure S3). The $[Cu^{2+}]_{aq}$ in the media changes from abundant at the beginning to depleted at the end of the 37 °C experiments with 5 μM Cu due to microbial uptake, which could trigger the "copper switch". In contrast, cells in the no-Cu experiment are always Cu-limited and therefore expressing sMMO, and that the high-Cu experiment is never Cu-limited and so cells express primarily pMMO.

In principle, it is possible that the change in net fractionation factors is a result of the change in the activity of pMMO versus sMMO. However, the change in net fractionation occurs in both the no-Cu and high-Cu experiments (Fig. 3C, 3D, 3G, 3H), indicating that the shift in net fractionation is unlikely to result from enzyme-specific effects. In the high-Cu experiment, the calculated net fractionation factors using data points with $f \geq 0.743$ are similar to the result of the 37°C ($f \geq 0.668$) experiment (Table 2). The two data points with $f \leq 0.328$ show the same isotopic depletion relative to the regression line derived from the points with higher f values, which is the same as the trend in the 37 °C experiment (Fig. 3C, 3D, 3G, 3H), so are not included in the regression. In the no-Cu experiment, even though the highest f value for the data points is 0.574 (Table 1, Fig. 2), which is the lower boundary of f values where fractionation factors change, the corresponding net fractionation factors calculated without time zero are very similar to 37 °C ($f \leq 0.556$) (Table 2, Fig. 3C, 3D, 3G, 3H).

The change in net fractionation factors correlates with the quantity of residual methane, not the change in copper availability. We show that the clumped isotope fractionation values are similar for pMMO-dominant (high-Cu) and sMMO-dominant (no-Cu) conditions, and that pMMO and sMMO do not have unique bulk carbon and hydrogen isotope fractionation factors, consistent with prior work (Feisthauer et al., 2011). It is therefore unlikely that enzyme-specific effects are significant contributors to the isotopic trajectories we observe for AeOM.

4.1.2. Hydrogen isotope exchange with water

Another putative mechanism for the observed divergence from Rayleigh fractionation (Fig. 3) is hydrogen isotope exchange between methane and water. In contrast to AOM, the first step of AeOM is generally considered irreversible and dominated by large kinetic isotope fractionations (Lee et al., 1993; Nesheim and Lipscomb, 1996). If isotope exchange between water and methane were to occur, the δD of methane should move towards the equilibrium values with water during the experiment. At 37 °C, the equilibrium fractionation factor between water and methane ($\alpha_{H_2O(l)-CH_4}$) is 1.260 (Horibe and Craig, 1995), which translates to 931 and 2181 ‰ for methane equilibrated with water having δD of 1433 and 3008 ‰, respectively. The observed δD of methane in the D-spiked experiments are well below the equilibrium values (Table 2). The other isotope signatures ($\delta^{13}C$, $\Delta^{13}CH_3D$ and $\Delta^{12}CH_2D_2$) of the D-spiked experiments are all similar to the results from the non-spiked 37 °C experiments (Fig. 2A, 2C, 2D). Therefore, we rule out the possibility of hydrogen isotope exchange with water.

4.1.3. Reservoir effect linked to methane transport and consumption

With the enzymatic effect and methane-water isotopic exchange ruled out, we consider a third potential mechanism — the reservoir effect in a closed-system. In other words, we consider that headspace methane and intracellular methane are distinct reservoirs. The measured isotopic signals are those for the headspace methane, the first reservoir, while the observed fractionation factors result from the combination of cross-membrane methane transport and methane oxidation, involving transport between the reservoirs and loss of methane to the second reservoir, respectively.

In order to examine this possibility, we construct and solve a two-box model to simulate the cross-membrane transport between methane inside and outside of the cells (Fig. 4). Following Nihous (2010), we assume that the cross-membrane transport (J_{in} and J_{out}) does not fractionate isotopes, but we do consider the possibility that rates change over the duration of the experiment. Methane is oxidized inside the cell, with an oxidation rate of $J_{oxidize}$. We assume that the intracellular oxidation has associated net isotope fractionation factors corresponding to those calculated at high f values, where reservoir effects are likely minimal. For simplicity, we assume methane concentrations inside the cells are at steady state, such that:

$$J_{in} - J_{out} = J_{oxidize} \tag{14}$$

The ratio between the methane oxidation rate $J_{oxidize}$ and the cross-membrane methane transport rate J_{in} can be described as a Damköhler number (Da) (Bailey et al., 2018):

$$\mathrm{Da} = \frac{\text{oxidation rate}}{\text{diffusive mass transfer rate}} = \frac{J_{oxidize}}{J_{in}} \tag{15}$$

where Da is a dimensionless number between 0 and 1, and higher Da values represent more methane oxidation relative to cross-membrane transport of methane.

For AeOM, only the first step of oxidation is considered since the reversibility of this step is low, suggesting that it is responsible for the rate of oxidation and associated kinetic isotope effects (Nesheim and Lipscomb, 1996). We adopt a reaction network similar to that utilized for AOM in Liu et al. (2023) (Table 3), with the modification that reactions are all assumed to be irreversible. This assumption is supported by the D-spiked experiments, as well as previous studies of AeOM (Lee et al., 1993). Therefore, only the reactions that break C-H or C-D bonds are accounted for in Table 3. The experimentally-derived net fractionation factors represent the ratios of rate constants between the

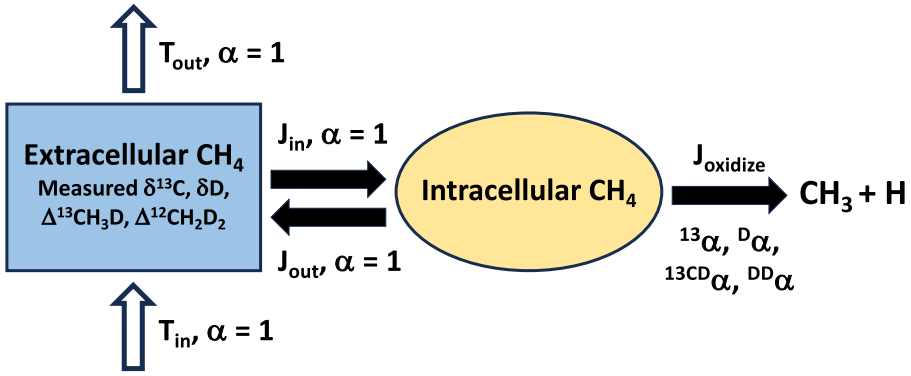

Fig. 4. An illustration of the two-box model developed in this study. The closed-system model only includes the solid arrows while the open-system model includes both the solid and hollow arrows. Methane is distinguished as extracellular methane (blue box) and intracellular methane (yellow box). The measured isotope signatures are the isotope compositions of extracellular methane. Cross-membrane transport rates are marked as J_{in} and J_{out} and assumed to have no isotope fractionation. Methane oxidation rate is represented by $J_{oxidize}$ and have the isotope fractionation derived from the experiments. The open-system model has additional advection input and output rates (T_{in} and T_{out}, shown as the hollow arrows) without isotope fractionation.

Table 3
Reactions, rate constants and fractionation factors used to calculate isotope fractionations during AeOM. The set of fractionation factors used for the 37 °C experiment is given as an example in the table. $K_{oxidize}$ is a tunable coefficient for controlling the oxidation rate $J_{oxidize}$. The relation between $K_{oxidize}$ and $J_{oxidize}$ is in the Supplementary Material.

Reaction	Rate constant	Fractionation factor	
$^{12}CH_4 \longrightarrow {}^{12}CH_3 + H$	$k_1 = K_{oxidize}\,\alpha_1$	$\alpha_1 = 1.0000$	(1)
$^{12}CH_3D \longrightarrow {}^{12}CH_3 + D$	$k_2 = 1/4\,K_{oxidize}\,{}^{D}\alpha$	${}^{D}\alpha = 0.6967$	(2)
$^{12}CH_3D \longrightarrow {}^{12}CH_2D + H$	$k_3 = 3/4\,K_{oxidize}\,{}^{D}\alpha$	${}^{D}\alpha = 0.6967$	(3)
$^{12}CH_2D_2 \longrightarrow {}^{12}CH_2D + D$	$k_4 = 1/2\,K_{oxidize}\,{}^{DD}\alpha$	${}^{DD}\alpha = 0.4309$	(4)
$^{12}CH_2D_2 \longrightarrow {}^{12}CHD_2 + H$	$k_5 = 1/2\,K_{oxidize}\,{}^{DD}\alpha$	${}^{DD}\alpha = 0.4309$	(5)
$^{13}CH_4 \longrightarrow {}^{13}CH_3 + H$	$k_6 = K_{oxidize}\,{}^{13}\alpha$	${}^{13}\alpha = 0.9671$	(6)
$^{13}CH_3D \longrightarrow {}^{13}CH_3 + D$	$k_7 = 1/4\,K_{oxidize}\,{}^{13CD}\alpha$	${}^{13CD}\alpha = 0.6716$	(7)
$^{13}CH_3D \longrightarrow {}^{13}CH_2D + H$	$k_8 = 3/4\,K_{oxidize}\,{}^{13CD}\alpha$	${}^{13CD}\alpha = 0.6716$	(8)

heavy isotopologues and $^{12}CH_4$. The measured net D/H fractionations are weighted convolutions of both primary and secondary fractionation effects (Ono et al., 2021; Liu et al., 2023). Due to the lack of data distinguishing primary and secondary isotope effects, we are unable to quantify the values of primary and secondary fractionation factors separately in this study. We note, however, that the overall isotope effects we calculate depend on the combination of primary and secondary fractionation factors that are embedded in our measured values. Therefore, our results are not affected by using a single fractionation factor rather than separate primary and secondary factors explicitly.

We further verified this by deconvolving these effects using experimentally derived primary and secondary fractionation factor ratios from Wilkins et al. (1994) and Nesheim and Lipscomb (1996), as shown in Table S3. The details in the calculations are described in the Supplementary Material. As expected, the results show that accounting for the primary and secondary fractionation factors has no effect on our results beyond rounding errors (Figure S4). Our simplification of using a single fractionation factor is therefore justified (e.g. Table 3, reactions 2 and 3), while recognizing that the single fractionation factor represents the combination of primary and secondary effects. The net fractionation factors from 37 °C ($f \geq 0.668$), 27 °C ($f \geq 0.374$) and 21 °C are taken as representative of the fractionation factors that are absent of reservoir effects, and they are assumed to be constant throughout each experiment. A set of ordinary differential equations (ODEs) is constructed to describe the time variation of methane isotopologues inside and outside the cells, and the numerical solutions are obtained at each time step (detailed in the Supplementary Material). The temporal change of abundances are then translated into the changes in isotopologue ratios with f.

We conducted a sensitivity test to examine how the ratio of the oxidation rate $J_{oxidize}$ relative to the transport rate J_{in} (i.e. Da) can influence the trajectory of isotope signatures. We change the value of either J_{in} or $J_{oxidize}$ while keeping the other constant (Fig. 5). To match the scale of experimental data, we use units of μmol/h for our rates. In the first test, we use J_{in} values of 500, 50, 30, 20, 10 and 5 μmol/h at a fixed $J_{oxidize}$ of 3.25 μmol/h (corresponding to $K_{oxidize} = 1$ in Table 3). In the second test, J_{in} is fixed at 20 μmol/h, while $J_{oxidize}$ varies, with values of 0.13, 1.30, 2.16, 3.25, 6.50 and 13.0 μmol/h. Therefore, the same set of Da (0.0065, 0.065, 0.108, 0.1625, 0.325 and 0.65) are used in the two tests, and the oxidation trajectories are shown in Fig. 5. For comparison, we use the Eqs. (10) and (11) to calculate the oxidation trajectory of a simple closed-system Rayleigh process.

The oxidation trajectories that share the same Da have the same pattern in both bulk and clumped isotope phase space (Fig. 5), illustrating that the relative magnitude of methane oxidation rate versus transport rate is the determining factor of the oxidation trajectories in this model. However, it is worth noticing that at a low methane oxidation rate, the total time to reach the same f is longer, which makes the reaction time an important factor to account for when fitting the experimental data. When the transport dominates the system (low Da), the oxidation trajectory is closer to a pure Rayleigh process (Fig. 5). This means the isotopically fractionated methane inside the cell is immediately expelled from the cell so that the isotopic composition of methane outside reflects only the isotope fractionation of the oxidation process. Conversely, in a transport-limited system (high Da), strongly fractionated methane gas is not immediately transported out of the cell, resulting in deviations from Rayleigh fractionation trajectories (i.e., there is a reservoir effect). As the transport rates decrease to values of the same order of magnitude as the oxidation rate (e.g. J_{in} decreases from 500 to 5 μmol/h, and Da number closer to 1), the trajectory deviates further from Rayleigh fractionation, eventually leading to a completely different direction in clumped isotope phase space (Fig. 5A and 5C). Departures from Rayleigh distillation are more significant in clumped isotope phase space (Fig. 5A and 5C) than in the bulk isotope phase space (Fig. 5B and 5D). Similar changes in net isotope fractionation factors that originate from changes in relative rates of

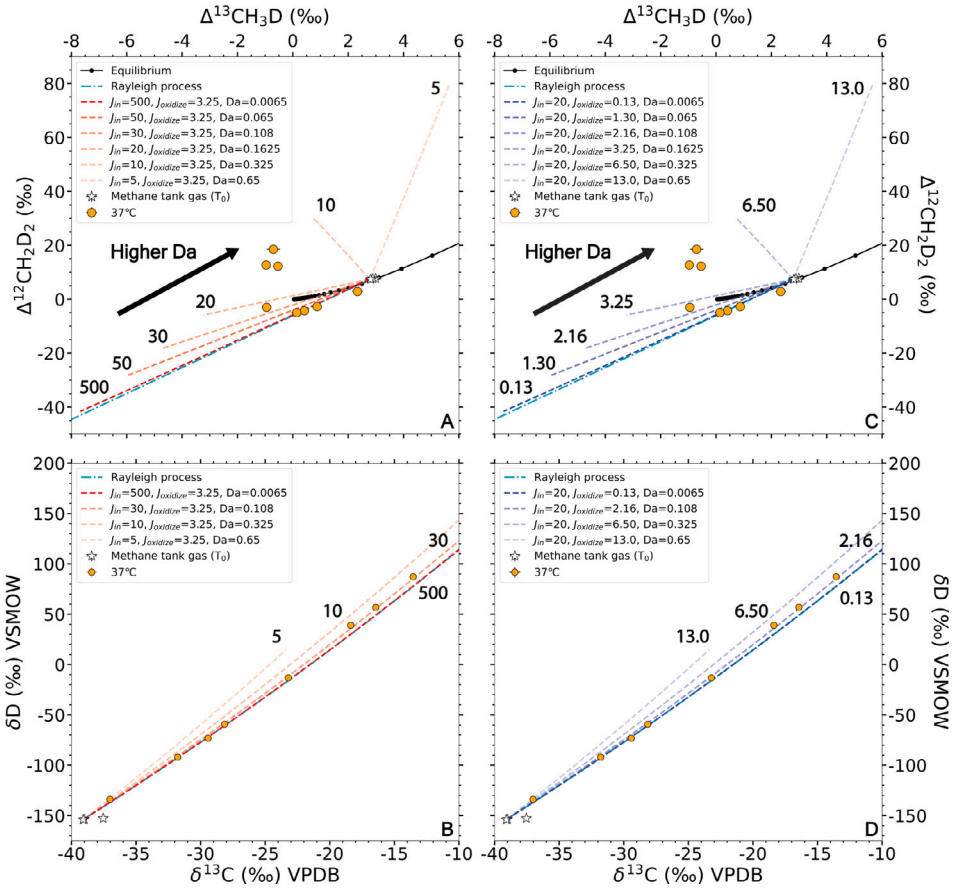

Fig. 5. Oxidation trajectories with different J_{in} and $J_{oxidize}$ values. Panels A and B are oxidation trajectories with varying J_{in} and constant $J_{oxidize}$ in clumped and bulk isotope phase spaces. Panels C and D are oxidation trajectories with varying $J_{oxidize}$ and constant J_{in} in clumped and bulk isotope phase spaces. Oxidation trajectories of pure Rayleigh processes are shown as cyan dashed lines. The numbers by the trajectories mark the values of varying rates. The arrows in panel A and C point to the direction of increasing Da. Variations between Da are less significant in bulk isotope phase space, thus only four curves with Da = 0.0065, 0.108, 0.325 and 0.65 are shown in panel B and D.

transport and consumption have been reported for bulk carbon isotope fractionation during microbial aerobic methane oxidation (Templeton et al., 2006) and for S isotopes during sulfate reduction (Wing and Halevy, 2014; Sim et al., 2017).

4.2. Constraints on the Damköhler number

Results from the box model indicate that varying Da over the course of the experiments allow us to best fit the isotopologue trajectories during methane oxidation in the 37 °C and 27 °C experiments. To illustrate, the $J_{oxidize}$ in Eq. (15) is set as the total methane oxidation rate calculated from the experimental data (Figure S1). We then assume that the cross-membrane transport is diffusion dominated, where the transport rate follows Fick's law. Given that the total methane transport J_{in} is under-constrained here, we parameterize Da using the following equation adopted from Clark et al. (2014):

$$\mathrm{Da} = \frac{J_{oxidize}}{J_{in}} = \frac{\frac{d[CH_4]}{dt}}{N_{cell}\frac{D}{R^2}[CH_4]_{outside}} \quad (16)$$

where $d[CH_4]/dt$ is the experimentally-derived total methane oxidation rate in μmol/h, and $[CH_4]_{outside}$ is the measured headspace methane concentration. The cell-specific cross-membrane diffusion rate is parameterized by the ratio of methane diffusivity (D) to the square of the radius of the cells (R), as well as by the headspace methane concentration. The total cross-membrane methane transport is obtained by multiplying the cell-specific rate with the total number of cells (N_{cell}). Assuming the diffusivity D is constant at a specific temperature, the temporal change in the total transport rate is attributable to changes in the number of cells (N_{cell}), the radius of the cells (R), as well as in the headspace methane concentration ($[CH_4]_{outside}$), which is monitored throughout the experiments. N_{cell} can be constrained by the OD_{600} of the culture (Mira et al., 2022). Since we lack the N_{cell} to OD_{600} calibration, we assume that N_{cell} is proportional to OD_{600} based on previous data (Zaarur et al., 2017; Mira et al., 2022):

$$OD_{600} = k_{cell} * N_{cell} \quad (17)$$

where k_{cell} is the linear conversion factor between OD_{600} and N_{cell}. The cell radii R is affected by several factors including the availability of nutrients and the growth stage of the cell (Chien et al., 2012), and thus more difficult to parameterize. In order to fit our experimental isotope data, and for simplicity, we assume that OD_{600} is proportional to R, which reflects the increase of cell size with microbial growth:

$$OD_{600} = k_R * R. \quad (18)$$

Similarly, k_R is the conversion factor between OD_{600} and R. With eqn. (17) and (18), Eq. (16) can be rewritten as:

$$\mathrm{Da} = \frac{\frac{d[CH_4]}{dt}}{\frac{D\,k_R^2}{k_{cell}}\frac{1}{OD_{600}}[CH_4]_{outside}} = \frac{\frac{d[CH_4]}{dt}}{\frac{k}{OD_{600}}[CH_4]_{outside}}. \quad (19)$$

The OD_{600} as a function of time in Eq. (19) is derived from the experimental data, as shown in Figure S5 A. k is a combination of constants k_R, k_{cell} and D. The value of k at each temperature is obtained from the best fit for the isotope data.

The model curves in bulk and clumped isotope phase space are shown in Fig. 6. The best-fit values for k are 0.14, 0.058 and 0.03

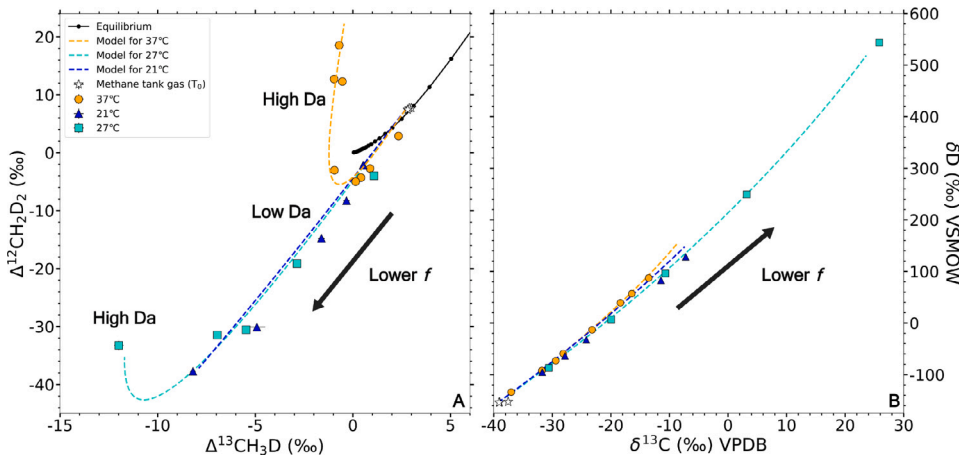

Fig. 6. Modeled oxidation trajectories in clumped (panel A) and bulk (panel B) isotope phase space. Data from the 37 °C, 27 °C and 21 °C experiments are fitted by the model. The parameterized $J_{oxidize}$, J_{in} and Da used for each curve are shown in Figure S5. The increases in $\Delta^{12}CH_2D_2$ values with f are due to increases in Da.

for the 37 °C, 27 °C and 21 °C experiments, respectively. Assuming k_{cell} and k_R are constant across all temperatures, the decrease of k with temperature indicates that D also decreases with temperature, consistent with the normal temperature dependence of diffusivity in general (Cussler, 2009). The model values for Da increase from 0.001 to 0.855, 0.00007 to 0.803, and 0.0015 to 0.061 in 37 °C, 27 °C and 21 °C experiments, respectively (Figure S5). This is due to a decrease in J_{in}, as well as an increase in $J_{oxidize}$ with microbial growth. $J_{oxidize}$ in the model increases linearly from 0.077 to a maximum of 3.79 μmol/h at 27 °C, while it increases as a fourth-order polynomial with time from 3.75 to a maximum of 30 μmol/h at 37 °C (see the Supplementary Material). These changes in rate are used to make the model integrated average methane oxidation rate match the observed total methane oxidation rate. In the 21 °C model, $J_{oxidize}$ is kept at a constant value of 0.96 μmol/h since the observed total methane oxidation rate is constant. Values for J_{in} decrease with time in all three models as a combined result of the increase in OD_{600} and the decrease in headspace methane amount (see Eq. (19) and Figure S1). It is worth highlighting that we are only providing one physically reasonable way to parameterize N_{cell} and R with OD_{600}, and uncertainties remain in the assumptions we made on the relationships between these three variables. Further tests show that the N_{cell}/R^2 proportional to values between $\frac{1}{OD_{600}}$ and $\frac{1}{OD_{600}^{1/2}}$ can fit the isotope data by scaling the constant k (see the Supplementary Materials). Assuming N_{cell} is proportional to OD_{600}, this corresponds to a 12 to 28 fold increase and a 7 to 13 fold increase in R for the 37 °C and 27 °C experiments, respectively. Despite these uncertainties in the parameterization of Da, the general conclusion that the increase of Da with the progression of the experiments results in the deviation from Rayleigh fractionation curves holds true.

In summary, the model indicates that in the 37 and 27 °C experiments, the magnitudes of oxidation rates are much smaller than transport rates at the beginning, but they become comparable to transport rates by the end of the experiments. In contrast, in the 21 °C experiment, the system remains dominated by transport rate throughout due to a low oxidation rate at the lower temperature.

4.3. Open system model with different cross-membrane transport

In many natural environments, aerobic microbial methane oxidation can occur in an open system as well. An example of such a system is methane diffusing up a stratified lake water column as described in Giunta et al. (2022). The $\Delta^{13}CH_3D$ and $\Delta^{12}CH_2D_2$ signatures of AeOM in an open-system with advection show different trends than those during closed-system AeOM. The influences of γ and the ratio between oxidation and advection (ϕ) were initially investigated by Wang et al. (2016) and Krause et al. (2022). Following the example of these previous works, we define ϕ as the ratio of methane oxidation rate and total advective input rate (Fig. 4):

$$\phi = \frac{J_{oxidize}}{T_{in}} \tag{20}$$

In this formulation, $\phi = 1$ represents a fully oxidative system in which all methane gas advected into the system is oxidized, while $\phi = 0$ represents a fully advective system in which all methane gas flows through the system without oxidation. The basic assumptions in the open-system model are: (1) the advection input (T_{in} in Fig. 4) has the same isotopic composition as the initial headspace methane; and (2) there is no isotope fractionation during advection. Based on the ODE set described in *section 4.4*, we construct a new ODE set by adding two terms for advection in and out of the system, and the numerical solutions are obtained as before. Since input and output rates are fixed, steady states between the reaction and the flow are attained. For the methane oxidation, we use the fractionation factors derived from the 37 °C experiment. The difference in whether distinguishing the primary and secondary isotope effect or not can be neglected (Figure S4), thus we are using the net fractionation factors here as well. We test the effect of the Damköhler number discussed in *section 4.4* on the steady-state clumped isotope signatures at different ϕ values (Fig. 7). The curves in Fig. 7 are not individual time series, but rather each point on the curve represents a steady-state clumped isotope signature in an open-system scenario with specific values for Da and ϕ. At the same Da, the effect of ϕ on clumped isotope ratios closely resembles the effect described in Krause et al. (2022), with higher ϕ values resulting in more positive $\Delta^{12}CH_2D_2$ values at steady state. Conversely, the effect of higher Da values at a fixed ϕ value is a more positive $\Delta^{13}CH_3D$ value. On the other hand, the effect of Da on $\Delta^{12}CH_2D_2$ is not unidirectional, marked by a less range of variation in $\Delta^{12}CH_2D_2$ value at high Da. However, the effect of Da is minor compared with ϕ and the general trend of higher ϕ having more positive $\Delta^{12}CH_2D_2$ values is not affected by different Da.

4.4. Implications

The results of this study reflect the sensitivity of the oxidation trajectory in clumped isotope phase space to net fractionation factors. Analogous results were obtained in some previous studies (Wang et al., 2016; Whitehill et al., 2017; Ono et al., 2021; Krause et al., 2022; Liu et al., 2023). Experimental data indicate that the variation of net fractionation factors in this study is unlikely to be the result of the change in relative activity of pMMO and sMMO nor the isotope re-equilibration between water and methane. We propose

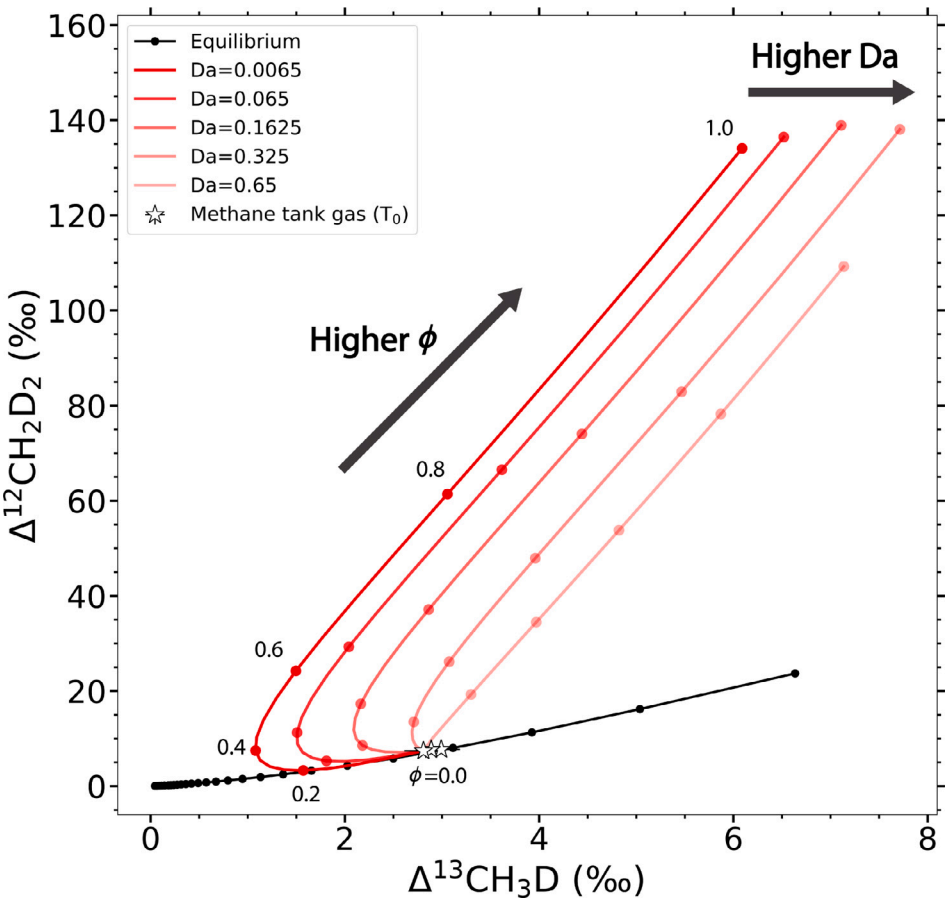

Fig. 7. Steady-state clumped isotope signatures in the open-system model. Each curve represents one value of Da, and each point on a curve represents a specific ϕ (marked by the number by the point). The directions of increasing ϕ and Da are shown by the two arrows in the figure.

that variations in fractionation factors can arise in closed systems by changes in the relative magnitudes of cross-membrane methane transport and methane oxidation rate (i.e., Damköhler number, Da). When transport rate is high relative to oxidation rate, the oxidation trajectory resembles Rayleigh fractionation, and the net fractionation factors are close to the fractionation factors of methane oxidation. However, the net fractionation factors shift towards unity when the transport rate is about the same order of magnitude as the oxidation rate, causing the oxidation trajectory to deviate significantly from a Rayleigh fractionation trend (Fig. 5). This effect is more prominent for $\Delta^{12}CH_2D_2$ as it reverses the sign of the trend (Fig. 5, Fig. 6). Therefore, the growth temperature (growth rate) does not alone control the clumped isotope ratios. Rather, temperature controls relative rates of oxidation and diffusion, which in turn determines the value for Da (Eq. (15)) and thus isotope fractionation. The combined result of cross-membrane transport and methane oxidation determines the isotopologue effects on residual methane, requiring a distinction be made between experimentally-derived fractionation factors and the actual fractionation factors of aerobic oxidation. Systems with low methane (or oxygen) concentration and fast methane consumption will exhibit large offsets between the fractionation factors intrinsic to the oxidation reaction and those observed.

Oxidation trajectories in methane clumped isotope space in closed systems at high Da values resemble those in an open-system oxidation trending towards steady state (Haghnegahdar et al., 2017; Whitehill et al., 2017; Krause et al., 2022; Haghnegahdar et al., 2023), both being characterized by very positive and increasing $\Delta^{12}CH_2D_2$ values. In our two-box model for closed systems (Fig. 4), the cells behave like the representative elementary volumes in open-system models in previous studies (Wang et al., 2016; Krause et al., 2022), but with an important difference: open-system models typically assume methane is advected into the system with constant isotopologue ratios, while in the closed system, the isotopologue concentrations of methane transported into the cells are changing. The isotopic signature of atmospheric methane oxidation can be better described by our two-box model for open systems (Fig. 7, Eq. (20)). T_{in} is the total methane emission rate into the troposphere and J_{in} is the methane transport rate from troposphere to stratosphere, and $J_{oxidize}$ is the methane oxidation rate by Cl and OH radicals in stratosphere. In this case, the open-system model results reflect the clumped isotope signatures of troposphere methane.

The recently reported clumped isotope compositions of atmospheric methane, which are strongly influenced by AeOM, show less positive $\Delta^{12}CH_2D_2$ values than expected from the models in which the source was assumed to be near isotopologue equilibrium (Haghnegahdar et al., 2023). This highlights the strong dependence of end-point isotopologue compositions on the initial composition. In our experiment, the initial methane tank gas is at thermodynamic equilibrium at a temperature of about 165 °C. If the initial methane isotopologue compositions begin with much lower $\Delta^{12}CH_2D_2$ values, in the microbial field, but follow the same oxidation trajectory as observed in this study, the resulting residual isotopologue compositions are expected to be near the equilibrium curve in mass-18 isotopologue space, with slightly positive $\Delta^{12}CH_2D_2$ values (Fig. 8). The same argument applies to the open-system model. Under these circumstances, methane gas from a microbial origin affected by AeOM will no longer show the indicative negative $\Delta^{12}CH_2D_2$ values typical for microbial methanogenesis (e.g., Young et al., 2017), but may instead exhibit positive $\Delta^{12}CH_2D_2$ values resembling either thermodynamic equilibrium, or even 'hyper-clumped' $\Delta^{12}CH_2D_2$ values, similar to atmospheric methane (Haghnegahdar et al., 2023). Our findings can be applied

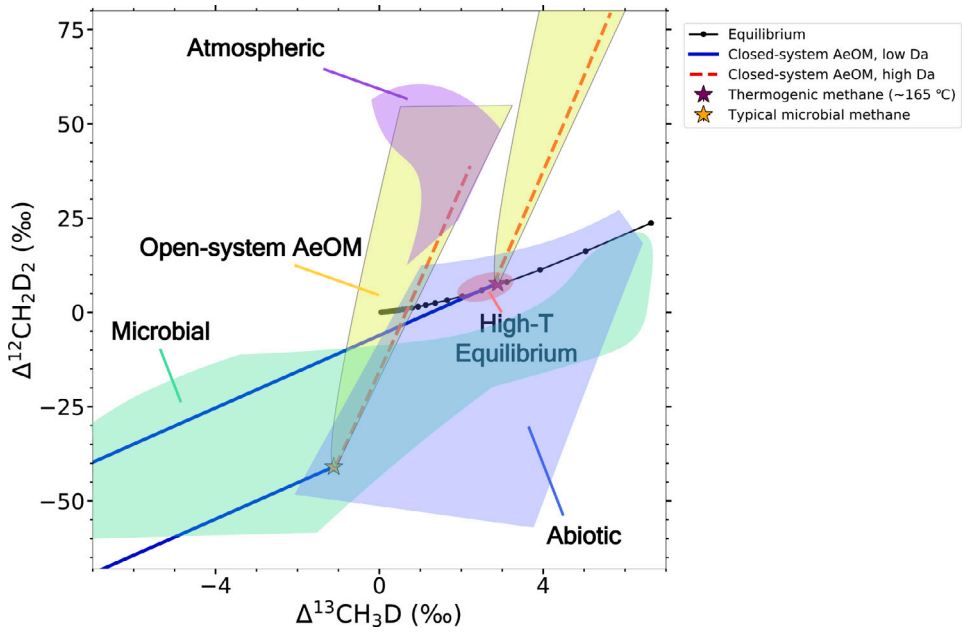

Fig. 8. A summary of the potential effects of AeOM on the original clumped isotope signatures. The fields of clumped isotope values are adopted from Young et al. (2019), Etiope and Oze (2022), Liu et al. (2023), and Haghnegahdar et al. (2023). Stars indicate the starting clumped compositions of either thermogenic methane equilibrated at 165 °C, or disequilibrated microbial methane with $\Delta^{13}CH_3D = -1$ ‰ and $\Delta^{12}CH_2D_2 = -41$ ‰. The red dashed lines and blue solid lines show the closed-system oxidation trajectories with high Da and low Da, respectively. The yellow shaded areas encompass the possible steady-state clumped isotope signatures of open-system AeOM.

in the future to tracking methane in natural and engineered systems where both microbiological production and oxidation occur, such as in deep and near subsurface fracture and hydrocarbon reservoirs, marine and lacustrine systems, and more recently, during carbon storage and methane removal (Young et al., 2017; Wang et al., 2018; Ash et al., 2019; Giunta et al., 2019; Thiagarajan et al., 2020; Nothaft et al., 2021; Warr et al., 2021; Tyne et al., 2021; Giunta et al., 2022; Bojanova et al., 2023; He et al., 2023).

Although the two-box model presented here fits the data very well, we are unable to quantify the variation of total methane transport with time in the experiments. Future studies with cell count, cell size and OD data, or direct quantification of methane uptake and oxidation (e.g. using isotopically-labeled methane) are necessary to test the model. Additionally, our model only accounts for total methane oxidation and transport, but cell-specific methane transport and methane oxidation rates may also influence the clumped isotope signatures, leaving considerable room for further study.

5. Conclusions

This study contributes to the development of methane clumped isotope as a tracer of methane cycling. Here we determined the role of growth rate on the isotope signatures ($\delta^{13}C$, δD, $\Delta^{13}CH_3D$ and $\Delta^{12}CH_2D_2$) of residual methane in closed-system aerobic biooxidation experiments. The results show variations of oxidation trajectory with growth rates. Further investigations indicate that the variation is independent of the primary oxidase enzyme (controlled by the copper concentration), nor due to the hydrogen exchange between methane and water. Rather, our model suggests that the variation is a result of the Damköhler number exerting a strong influence on the clumped isotope signatures in closed systems. While our model indicates that the general clumped isotopologue trend of open-system methane oxidation is not significantly affected by the Damköhler number, methane oxidation in many natural environments occurs in partly or mostly closed systems. Therefore, our findings will have broad application in future studies.

The results of this study underscore the role microbial activity plays in setting the bulk and clumped isotope compositions of methane in Earths atmosphere. With these estimates of aerobic methane fractionation, we add a tool with which to diagnose the provenance of methane in environments where methane and oxygen are available for microbial respiration. Future studies on the relationship between rates of methane transport versus oxidation are required to validate the model developed above.

CRediT authorship contribution statement

Jiawen Li: Writing – review & editing, Writing – original draft, Visualization, Validation, Software, Methodology, Investigation, Formal analysis, Data curation, Conceptualization. **Beverly K. Chiu:** Writing – original draft, Methodology, Formal analysis, Data curation, Conceptualization. **Alison M. Piasecki:** Writing – original draft, Methodology, Investigation, Conceptualization. **Xiahong Feng:** Writing – review & editing, Writing – original draft, Validation, Methodology, Formal analysis, Data curation. **Joshua D. Landis:** Writing – original draft, Methodology, Formal analysis, Data curation. **Sarah Marcum:** Writing – original draft, Formal analysis. **Edward D. Young:** Writing – review & editing, Writing – original draft, Supervision, Resources, Project administration, Funding acquisition, Conceptualization. **William D. Leavitt:** Writing – review & editing, Writing – original draft, Supervision, Project administration, Funding acquisition, Formal analysis, Conceptualization.

Declaration of competing interest

The authors declare that they have no known competing financial interests or personal relationships that could have appeared to influence the work reported in this paper.

Data availability

Data and codes are available through GitLab at https://git.dartmouth.edu/leavitt_lab/aerobic_methanotroph and figshare at https://figshare.com/projects/Li_etal_2024_AeOM/184504.

Acknowledgments

This research was supported by funding from NASA, United States grant 80NSSC21K0477 (EDY, WDL) and the Simons Foundation Award, United States #623881 (WDL). We thank Whitney Thomas, Carolynn Harris and Jiarui Liu for assistance with lab experiments and thank Jeemin Rhim for the insightful discussions on the project. We thank Shuhei Ono for editorial handling, as well as David Wang, Naizhong Zhang, and an anonymous reviewer for the valuable insight that improved an earlier version of this manuscript.

Appendix A. Supplementary data

The supplementary material includes the ordinary differential equation set and the parameters used in the two-box model, the calculations of primary and secondary isotope fractionation factors, supplementary figures S1-S6, and supplementary tables S1-S3.

Supplementary material related to this article can be found online at https://doi.org/10.1016/j.gca.2024.06.032.

References

Ash, J., Egger, M., Treude, T., Kohl, I., Cragg, B., Parkes, R.J., Slomp, C., Sherwood Lollar, B., Young, E.D., 2019. Exchange catalysis during anaerobic methanotrophy revealed by 12CH2D2 and 13CH3D in methane. Geochem. Perspect. Lett. 10, 26–30.

Bailey, J.E., Ollis, D.F., et al., 2018. Biochemical Engineering Fundamentals. McGraw-Hill.

Bigeleisen, J., 1955. Statistical mechanics of isotopic systems with small quantum corrections. I. General considerations and the rule of the geometric mean. J. Chem. Phys. 23 (12), 2264–2267.

Bojanova, D.P., De Anda, V.Y., Haghnegahdar, M.A., Teske, A.P., Ash, J.L., Young, E.D., Baker, B.J., LaRowe, D.E., Amend, J.P., 2023. Well-hidden methanogenesis in deep, organic-rich sediments of guaymas basin. ISME J. 17 (11), 1828–1838.

Bowman, J.P., 2014. The Family methylococcaceae. In: Rosenberg, E., DeLong, E.F., Lory, S., Stackebrandt, E., Thompson, F. (Eds.), The Prokaryotes: Gammaproteobacteria. Springer Berlin Heidelberg, Berlin, Heidelberg, pp. 411–440.

Brock, T.D., Madigan, M.T., Martinko, J.M., Parker, J., 2003. Brock Biology of Microorganisms. Prentice-Hall, Upper Saddle River (NJ).

Cao, X., Liu, Y., 2012. Theoretical estimation of the equilibrium distribution of clumped isotopes in nature. Geochim. Cosmochim. Acta 77, 292–303.

Catling, D.C., Zahnle, K.J., McKay, C.P., 2001. Biogenic methane, hydrogen escape, and the irreversible oxidation of early Earth. Science 293 (5531), 839–843.

Chien, A.-C., Hill, N.S., Levin, P.A., 2012. Cell size control in bacteria. Curr. Biol. 22 (9), R340–R349.

Cicerone, R.J., Oremland, R.S., 1988. Biogeochemical aspects of atmospheric methane. Glob. Biogeochem. Cycles 2 (4), 299–327.

Clark, R.L., Cameron, J.C., Root, T.W., Pfleger, B.F., 2014. Insights into the industrial growth of cyanobacteria from a model of the carbon-concentrating mechanism. AIChE J. 60 (4), 1269–1277.

Colby, J., Stirling, D.I., Dalton, H., 1977. The soluble methane mono-oxygenase of *Methylococcus capsulatus* (Bath). Its ability to oxygenate *n*-alkanes, n-alkenes, ethers, and alicyclic, aromatic and heterocyclic compounds. Biochem. J. 165 (2), 395–402.

Coleman, D.D., Risatti, J., Schoell, M., 1981. Fractionation of carbon and hydrogen isotopes by methane-oxidizing bacteria. Geochim. Cosmochim. Acta 45 (7), 1033–1037.

Curry, C.L., 2007. Modeling the soil consumption of atmospheric methane at the global scale. Glob. Biogeochem. Cycles 21 (4).

Cussler, E.L., 2009. Diffusion: Mass Transfer in Fluid Systems. Cambridge University Press.

Dlugokencky, E.J., Nisbet, E.G., Fisher, R., Lowry, D., 2011. Global atmospheric methane: budget, changes and dangers. Phil. Trans. R. Soc. A 369 (1943), 2058–2072.

Douglas, P.M., Stolper, D.A., Eiler, J.M., Sessions, A.L., Lawson, M., Shuai, Y., Bishop, A., Podlaha, O.G., Ferreira, A.A., Santos Neto, E.V., Niemann, M., Steen, A.S., Huang, L., Chimiak, L., Valentine, D.L., Fiebig, J., Luhmann, A.J., Seyfried, W.E., Etiope, G., Schoell, M., Inskeep, W.P., Moran, J.J., Kitchen, N., 2017. Methane clumped isotopes: Progress and potential for a new isotopic tracer. Org. Geochem. 113, 262–282.

Douglas, P., Stolper, D., Smith, D., Walter Anthony, K., Paull, C., Dallimore, S., Wik, M., Crill, P., Winterdahl, M., Eiler, J., Sessions, A., 2016. Diverse origins of Arctic and Subarctic methane point source emissions identified with multiply-substituted isotopologues. Geochim. Cosmochim. Acta 188, 163–188.

Ehhalt, D.H., 1974. The atmospheric cycle of methane. Tellus 26 (1–2), 58–70.

Eldridge, D.L., Korol, R., Lloyd, M.K., Turner, A.C., Webb, M.A., Miller, T.F., Stolper, D.A., 2019. Comparison of experimental vs theoretical abundances of 13CH3D and 12CH2D2 for isotopically equilibrated systems from 1 to 500 °C. ACS Earth Space Chem. 3 (12), 2747–2764.

Etiope, G., Oze, C., 2022. Microbial vs abiotic origin of methane in continental serpentinized ultramafic rocks: A critical review and the need of a holistic approach. Appl. Geochem. 143, 105373.

Etiope, G., Sherwood Lollar, B., 2013. Abiotic methane on Earth. Rev. Geophys. 51 (2), 276–299.

Faramawy, S., Zaki, T., Sakr, A.-E., 2016. Natural gas origin, composition, and processing: A review. J. Nat. Gas Sci. Eng. 34, 34–54.

Feisthauer, S., Vogt, C., Modrzynski, J., Szlenkier, M., Krüger, M., Siegert, M., Richnow, H.-H., 2011. Different types of methane monooxygenases produce similar carbon and hydrogen isotope fractionation patterns during methane oxidation. Geochim. Cosmochim. Acta 75 (5), 1173–1184.

Frieling, J., Svensen, H.H., Planke, S., Cramwinckel, M.J., Selnes, H., Sluijs, A., 2016. Thermogenic methane release as a cause for the long duration of the PETM. Proc. Natl. Acad. Sci. 113 (43), 12059–12064.

Gassner, G.T., Lippard, S.J., 1999. Component interactions in the soluble methane monooxygenase system from *Methylococcus capsulatus* (Bath). Biochemistry 38 (39), 12768–12785.

Giunta, T., Young, E.D., Labidi, J., Sansjofre, P., Jézéquel, D., Donval, J.-P., Brandily, C., Ruffine, L., 2022. Extreme methane clumped isotopologue bio-signatures of aerobic and anaerobic methanotrophy: Insights from the Lake Pavin and the Black Sea sediments. Geochim. Cosmochim. Acta 338, 34–53.

Giunta, T., Young, E.D., Warr, O., Kohl, I., Ash, J.L., Martini, A., Mundle, S.O., Rumble, D., Pérez-Rodríguez, I., Wasley, M., LaRowe, D.E., Gilbert, A., Sherwood Lollar, B., 2019. Methane sources and sinks in continental sedimentary systems: New insights from paired clumped isotopologues 13CH3D and 12CH2D2. Geochim. Cosmochim. Acta 245, 327–351.

Gonzalez, Y., Nelson, D.D., Shorter, J.H., McManus, J.B., Dyroff, C., Formolo, M., Wang, D.T., Western, C.M., Ono, S., 2019. Precise measurements of 12CH2D2 by tunable infrared laser direct absorption spectroscopy. Anal. Chem. 91 (23), 14967–14974.

Greening, C., Grinter, R., 2022. Microbial oxidation of atmospheric trace gases. Nat. Rev. Microbiol. 20 (9), 513–528.

Gruen, D.S., Wang, D.T., Könneke, M., Topçuoğlu, B.D., Stewart, L.C., Goldhammer, T., Holden, J.F., Hinrichs, K.-U., Ono, S., 2018. Experimental investigation on the controls of clumped isotopologue and hydrogen isotope ratios in microbial methane. Geochim. Cosmochim. Acta 237, 339–356.

Haghnegahdar, M.A., Schauble, E.A., Young, E.D., 2017. A model for 12CH2D2 and 13CH3D as complementary tracers for the budget of atmospheric CH4. Glob. Biogeochem. Cycles 31 (9), 1387–1407.

Haghnegahdar, M.A., Sun, J., Hultquist, N., Hamovit, N.D., Kitchen, N., Eiler, J., Ono, S., Yarwood, S.A., Kaufman, A.J., Dickerson, R.R., et al., 2023. Tracing sources of atmospheric methane using clumped isotopes. Proc. Natl. Acad. Sci. 120 (47), e2305574120.

Hamak, J.E., Sigler, S., 1991. Analyses of Natural Gases, 1986-90, Vol. 9301. US Department of the Interior, Bureau of Mines.

Hanson, R.S., Hanson, T.E., 1996. Methanotrophic bacteria. Microbiological reviews 60 (2), 439–471.

He, L., Groom, J.D., Wilson, E.H., Fernandez, J., Konopka, M.C., Beck, D.A., Lidstrom, M.E., 2023. A methanotrophic bacterium to enable methane removal for climate mitigation. Proc. Natl. Acad. Sci. 120 (35), e2310046120.

Horibe, Y., Craig, H., 1995. DH fractionation in the system methane-hydrogen-water. Geochim. Cosmochim. Acta 59 (24), 5209–5217.

Kawagucci, S., Matsui, Y., Makabe, A., Fukuba, T., Onishi, Y., Nunoura, T., Yokokawa, T., 2021. Hydrogen and carbon isotope fractionation factors of aerobic methane oxidation in deep-sea water. Biogeosciences 18 (19), 5351–5362.

Kirschke, S., Bousquet, P., Ciais, P., Saunois, M., Canadell, J.G., Dlugokencky, E.J., Bergamaschi, P., Bergmann, D., Blake, D.R., Bruhwiler, L., Cameron-Smith, P., Castaldi, S., Chevallier, F., Feng, L., Fraser, A., Heimann, M., Hodson, E.L., Houweling, S., Josse, B., Fraser, P.J., Krummel, P.B., Lamarque, J.-F., Langenfelds, R.L., Le Quéré, C., Naik, V., O'Doherty, S., Palmer, P.I., Pison, I., Plummer, D., Poulter, B., Prinn, R.G., Rigby, M., Ringeval, B., Santini, M., Schmidt, M., Shindell, D.T., Simpson, I.J., Spahni, R., Steele, L.P., Strode, S.A., Sudo, K., Szopa, S., Werf, G.R. Van Der, Voulgarakis, A., Van Weele, M., Weiss, R.F., Williams, J.E., Zeng, G., 2013. Three decades of global methane sources and sinks. Nat. Geosci. 6 (10), 813–823.

Koo, C.W., Rosenzweig, A.C., 2021. Biochemistry of aerobic biological methane oxidation. Chem. Soc. Rev. 50 (5), 3424–3436.

Kopec, B.G., Feng, X., Posmentier, E.S., Sonder, L.J., 2019. Seasonal Deuterium Excess Variations of Precipitation at Summit, Greenland, and their Climatological Significance. J. Geophys. Res.: Atmos. 124 (1), 72–91.

Krause, S.J., Liu, J., Young, E.D., Treude, T., 2022. Δ13CH3D and Δ12CH2D2 signatures of methane aerobically oxidized by methylosinus trichosporium with implications for deciphering the provenance of methane gases. Earth Planet. Sci. Lett. 593, 117681.

Labidi, J., Young, E.D., Giunta, T., Kohl, I.E., Seewald, J., Tang, H., Lilley, M.D., Früh-Green, G.L., 2020. Methane thermometry in deep-sea hydrothermal systems: evidence for re-ordering of doubly-substituted isotopologues during fluid cooling. Geochim. Cosmochim. Acta 288, 248–261.

Landis, J.D., Renshaw, C.E., Kaste, J.M., 2021. Sorption behavior and aerosol–particulate transitions of ^{7} Be, ^{10} Be, and ^{210} Pb: A basis for fallout radionuclide chronometry. Environ. Sci. Technol. 55 (21), 14957–14967.

Laws, E.A., Popp, B.N., Bidigare, R.R., Kennicutt, M.C., Macko, S.A., 1995. Dependence of phytoplankton carbon isotopic composition on growth rate and [co2) aq: theoretical considerations and experimental results. Geochim. Cosmochim. Acta 59 (6), 1131–1138.

Leavitt, W.D., Halevy, I., Bradley, A.S., Johnston, D.T., 2013. Influence of sulfate reduction rates on the phanerozoic sulfur isotope record. Proc. Natl. Acad. Sci. 110 (28), 11244–11249.

Lee, S., Nesheim, J., Lipscomb, J., 1993. Transient intermediates of the methane monooxygenase catalytic cycle. J. Biol. Chem. 268 (29), 21569–21577.

Liu, J., Harris, R.L., Ash, J.L., Ferry, J.G., Krause, S.J., Labidi, J., Prakash, D., Lollar, B.S., Treude, T., Warr, O., 2023. Reversibility controls on extreme methane clumped isotope signatures from anaerobic oxidation of methane. Geochim. Cosmochim. Acta 348, 165–186.

Liu, Q., Liu, Y., 2016. Clumped-isotope signatures at equilibrium of CH4, NH3, H2O, H2S and SO2. Geochim. Cosmochim. Acta 175, 252–270.

Mao, S.-H., Zhang, H.-H., Zhuang, G.-C., Li, X.-J., Liu, Q., Zhou, Z., Wang, W.-L., Li, C.-Y., Lu, K.-Y., Liu, X.-T., Montgomery, A., Joye, S.B., Zhang, Y.-Z., Yang, G.-P., 2022. Aerobic oxidation of methane significantly reduces global diffusive methane emissions from shallow marine waters. Nature Commun. 13 (1), 7309.

Mariotti, A., Germon, J.C., Hubert, P., Kaiser, P., Letolle, R., Tardieux, A., Tardieux, P., 1981. Experimental determination of nitrogen kinetic isotope fractionation: Some principles; illustration for the denitrification and nitrification processes. Plant Soil 62 (3), 413–430.

McCollom, T.M., Seewald, J.S., 2001. A reassessment of the potential for reduction of dissolved CO2 to hydrocarbons during serpentinization of olivine. Geochim. Cosmochim. Acta 65 (21), 3769–3778.

McKay, C.P., Porco, C.C., Altheide, T., Davis, W.L., Kral, T.A., 2008. The possible origin and persistence of life on enceladus and detection of biomarkers in the plume. Astrobiology 8 (5), 909–919.

McKay, C., Smith, H., 2005. Possibilities for methanogenic life in liquid methane on the surface of Titan. Icarus 178 (1), 274–276.

Mira, P., Yeh, P., Hall, B.G., 2022. Estimating microbial population data from optical density. PLoS One 17 (10), e0276040.

Nesheim, J.C., Lipscomb, J.D., 1996. Large kinetic isotope effects in methane oxidation catalyzed by methane monooxygenase: evidence for C-H bond cleavage in a reaction cycle intermediate. Biochemistry 35 (31), 10240–10247.

Nielsen, A.K., Gerdes, K., Murrell, J.C., 1997. Copper-dependent reciprocal transcriptional regulation of methane monooxygenase genes in *Methylococcus capsulatus* and *Methylosinus trichosporium*. Mol. Microbiol. 25 (02), 399–409.

Nihous, G.C., 2010. Notes on the temperature dependence of carbon isotope fractionation by aerobic CH_4 -oxidising bacteria. Isot. Environ. Health Stud. 46 (2), 133–140.

Nothaft, D.B., Templeton, A.S., Rhim, J.H., Wang, D.T., Labidi, J., Miller, H.M., Boyd, E.S., Matter, J.M., Ono, S., Young, E.D., et al., 2021. Geochemical, biological, and clumped isotopologue evidence for substantial microbial methane production under carbon limitation in serpentinites of the samail ophiolite, oman. J. Geophys. Res. Biogeosci. 126 (10), e2020JG006025.

Ono, S., Rhim, J.H., Gruen, D.S., Taubner, H., Kölling, M., Wegener, G., 2021. Clumped isotopologue fractionation by microbial cultures performing the anaerobic oxidation of methane. Geochim. Cosmochim. Acta 293, 70–85.

Oremland, R.S., Culbertson, C.W., 1992. Importance of methane-oxidizing bacteria in the methane budget as revealed by the use of a specific inhibitor. Nature 356 (6368), 421–423.

Prior, S.D., Dalton, H., 1985. The effect of copper ions on membrane content and methane monooxygenase activity in methanol-grown cells of Methylococcus capsulatus (Bath). Microbiology 131 (1), 155–163.

Qin, Q., Kinnaman, F.S., Gosselin, K.M., Liu, N., Treude, T., Valentine, D.L., 2022. Seasonality of water column methane oxidation and deoxygenation in a dynamic marine environment. Geochim. Cosmochim. Acta 336, 219–230.

Rasigraf, O., Vogt, C., Richnow, H.-H., Jetten, M.S., Ettwig, K.F., 2012. Carbon and hydrogen isotope fractionation during nitrite-dependent anaerobic methane oxidation by Methylomirabilis oxyfera. Geochim. Cosmochim. Acta 89, 256–264.

Ribbons, D., Michalover, J., 1970. Methane oxidation by cell-free extracts of Methylococcus capsulatus. FEBS Lett. 11 (1), 41–44.

Ross, M.O., Rosenzweig, A.C., 2017. A tale of two methane monooxygenases. JBIC J. Biol. Inorg. Chem. 22 (2–3), 307–319.

Ruppel, C.D., Kessler, J.D., 2017. The interaction of climate change and methane hydrates. Rev. Geophys. 55 (1), 126–168.

Saunois, M., Stavert, A.R., Poulter, B., Bousquet, P., Canadell, J.G., Jackson, R.B., Raymond, P.A., Dlugokencky, E.J., Houweling, S., Patra, P.K., Ciais, P., Arora, V.K., Bastviken, D., Bergamaschi, P., Blake, D.R., Brailsford, G., Bruhwiler, L., Carlson, K.M., Carrol, M., Castaldi, S., Chandra, N., Crevoisier, C., Crill, P.M., Covey, K., Curry, C.L., Etiope, G., Frankenberg, C., Gedney, N., Hegglin, M.I., Höglund-Isaksson, L., Hugelius, G., Ishizawa, M., Ito, A., Janssens-Maenhout, G., Jensen, K.M., Joos, F., Kleinen, T., Krummel, P.B., Langenfelds, R.L., Laruelle, G.G., Liu, L., Machida, T., Maksyutov, S., McDonald, K.C., McNorton, J., Miller, P.A., Melton, J.R., Morino, I., Müller, J., Murguia-Flores, F., Naik, V., Niwa, Y., Noce, S., O'Doherty, S., Parker, R.J., Peng, C., Peng, S., Peters, G.P., Prigent, C., Prinn, R., Ramonet, M., Regnier, P., Riley, W.J., Rosentreter, J.A., Segers, A., Simpson, I.J., Shi, H., Smith, S.J., Steele, L.P., Thornton, B.F., Tian, H., Tohjima, Y., Tubiello, F.N., Tsuruta, A., Viovy, N., Voulgarakis, A., Weber, T.S., Van Weele, M., Van Der Werf, G.R., Weiss, R.F., Worthy, D., Wunch, D., Yin, Y., Yoshida, Y., Zhang, W., Zhang, Z., Zhao, Y., Zheng, B., Zhu, Q., Zhu, Q., Zhuang, Q., 2020. The Global Methane Budget 2000–2017. Earth Syst. Sci. Data 12 (3), 1561–1623.

Schoell, M., 1988. Multiple origins of methane in the Earth. Chem. Geol. 71 (1–3), 1–10.

Sim, M.S., Paris, G., Adkins, J.F., Orphan, V.J., Sessions, A.L., 2017. Quantification and isotopic analysis of intracellular sulfur metabolites in the dissimilatory sulfate reduction pathway. Geochim. Cosmochim. Acta 206, 57–72.

Sirajuddin, S., Rosenzweig, A.C., 2015. Enzymatic Oxidation of Methane. Biochemistry 54 (14), 2283–2294.

Stanley, S.H., Prior, S.D., Leak, D.J., Dalton, H., 1983. Copper stress underlies the fundamental change in intracellular location of methane mono-oxygenase in methane-oxidizing organisms: Studies in batch and continuous cultures. Biotechnol. Lett. 5 (7), 487–492.

Stolper, D., Lawson, M., Davis, C., Ferreira, A., Neto, E.S., Ellis, G., Lewan, M., Martini, A.M., Tang, Y., Schoell, M., 2014. Formation temperatures of thermogenic and biogenic methane. Science 344 (6191), 1500–1503.

Stolper, D., Martini, A., Clog, M., Douglas, P., Shusta, S., Valentine, D., Sessions, A., Eiler, J., 2015. Distinguishing and understanding thermogenic and biogenic sources of methane using multiply substituted isotopologues. Geochim. Cosmochim. Acta 161, 219–247.

Taenzer, L., Labidi, J., Masterson, A.L., Feng, X., Rumble, III, D., Young, E.D., Leavitt, W.D., 2020. Low Δ12CH2D2 values in microbialgenic methane result from combinatorial isotope effects. Geochim. Cosmochim. Acta 285, 225–236.

Templeton, A.S., Chu, K.-H., Alvarez-Cohen, L., Conrad, M.E., 2006. Variable carbon isotope fractionation expressed by aerobic CH4-oxidizing bacteria. Geochim. Cosmochim. Acta 70 (7), 1739–1752.

Thiagarajan, N., Kitchen, N., Xie, H., Ponton, C., Lawson, M., Formolo, M., Eiler, J., 2020. Identifying thermogenic and microbial methane in deep water Gulf of Mexico Reservoirs. Geochim. Cosmochim. Acta 275, 188–208.

Thompson, M.A., Krissansen-Totton, J., Wogan, N., Telus, M., Fortney, J.J., 2022. The case and context for atmospheric methane as an exoplanet biosignature. Proc. Natl. Acad. Sci. 119 (14), e2117933119.

Thottathil, S.D., Reis, P.C.J., Prairie, Y.T., 2022. Variability and controls of stable carbon isotopic fractionation during aerobic methane oxidation in temperate lakes. Front. Environ. Sci. 10, 833688.

Tyne, R., Barry, P., Lawson, M., Byrne, D., Warr, O., Xie, H., Hillegonds, D., Formolo, M., Summers, Z., Skinner, B., et al., 2021. Rapid microbial methanogenesis during co2 storage in hydrocarbon reservoirs. Nature 600 (7890), 670–674.

Wang, D.T., Gruen, D.S., Lollar, B.S., Hinrichs, K.-U., Stewart, L.C., Holden, J.F., Hristov, A.N., Pohlman, J.W., Morrill, P.L., Könneke, M., 2015. Nonequilibrium clumped isotope signals in microbial methane. Science 348 (6233), 428–431.

Wang, D.T., Reeves, E.P., McDermott, J.M., Seewald, J.S., Ono, S., 2018. Clumped isotopologue constraints on the origin of methane at seafloor hot springs. Geochim. Cosmochim. Acta 223, 141–158.

Wang, Z., Schauble, E.A., Eiler, J.M., 2004. Equilibrium thermodynamics of multiply substituted isotopologues of molecular gases. Geochim. Cosmochim. Acta 68 (23), 4779–4797.

Wang, D.T., Welander, P.V., Ono, S., 2016. Fractionation of the methane isotopologues 13CH4, 12CH3D, and 13CH3D during aerobic oxidation of methane by *Methylococcus capsulatus* (Bath). Geochim. Cosmochim. Acta 192, 186–202.

Warr, O., Young, E.D., Giunta, T., Kohl, I.E., Ash, J.L., Sherwood Lollar, B., 2021. High-resolution, long-term isotopic and isotopologue variation identifies the sources and sinks of methane in a deep subsurface carbon cycle. Geochim. Cosmochim. Acta 294, 315–334.

Welander, P.V., Summons, R.E., 2012. Discovery, taxonomic distribution, and phenotypic characterization of a gene required for 3-methylhopanoid production. Proc. Natl. Acad. Sci. 109 (32), 12905–12910.

Whitehill, A.R., Joelsson, L.M.T., Schmidt, J.A., Wang, D.T., Johnson, M.S., Ono, S., 2017. Clumped isotope effects during OH and Cl oxidation of methane. Geochim. Cosmochim. Acta 196, 307–325.

Whiticar, M.J., 1999. Carbon and hydrogen isotope systematics of bacterial formation and oxidation of methane. Chem. Geol. 161 (1–3), 291–314.

Wilkins, P.C., Dalton, H., Samuel, C.J., Green, J., 1994. Further evidence for multiple pathways in soluble methane-monooxygenase-catalysed oxidations from the measurement of deuterium kinetic isotope effects. Eur. J. Biochem. 226 (2), 555–560.

Wing, B.A., Halevy, I., 2014. Intracellular metabolite levels shape sulfur isotope fractionation during microbial sulfate respiration. Proc. Natl. Acad. Sci. 111 (51), 18116–18125.

Yamamoto, S., Alcauskas, J.B., Crozier, T.E., 1976. Solubility of methane in distilled water and seawater. J. Chem. Eng. 21 (1), 78–80.

York, D., Evensen, N.M., Martínez, M.L., De Basabe Delgado, J., 2004. Unified equations for the slope, intercept, and standard errors of the best straight line. Am. J. Phys. 72 (3), 367–375.

Young, E.D., Kohl, I.E., Lollar, B.S., Etiope, G., Rumble, III, D., Li, S., Haghnegahdar, M.A., Schauble, E.A., McCain, K., Foustoukos, D., et al., 2017. The relative abundances of resolved 12CH2D2 and 13CH3D and mechanisms controlling isotopic bond ordering in abiotic and biotic methane gases. Geochim. Cosmochim. Acta 203, 235–264.

Young, E., Orcutt, B., Daniel, I., Dasgupta, R., 2019. A two-dimensional perspective on CH4 isotope clumping. In: Deep Carbon, vol. 1029, Cambridge University Press Cambridge, Publisher, pp. 388–414.

Young, E.D., Rumble, III, D., Freedman, P., Mills, M., 2016. A large-radius high-mass-resolution multiple-collector isotope ratio mass spectrometer for analysis of rare isotopologues of O2, N2, CH4 and other gases. Int. J. Mass Spectrom. 401, 1–10.

Yung, Y.L., Chen, P., Nealson, K., Atreya, S., Beckett, P., Blank, J.G., Ehlmann, B., Eiler, J., Etiope, G., Ferry, J.G., Forget, F., Gao, P., Hu, R., Kleinböhl, A., Kluseman, R., Lefèvre, F., Miller, C., Mischna, M., Mumma, M., Newman, S., Oehler, D., Okumura, M., Oremland, R., Orphan, V., Popa, R., Russell, M., Shen, L., Sherwood Lollar, B., Staehle, R., Stamenković, V., Stolper, D., Templeton, A., Vandaele, A.C., Viscardy, S., Webster, C.R., Wennberg, P.O., Wong, M.L., Worden, J., 2018. Methane on mars and habitability: Challenges and responses. Astrobiology 18 (10), 1221–1242.

Zaarur, S., Wang, D.T., Ono, S., Bosak, T., 2017. Influence of phosphorus and cell geometry on the fractionation of sulfur isotopes by several species of desulfovibrio during microbial sulfate reduction. Front. Microbiol. 8 (890).

Zhang, N., Snyder, G.T., Lin, M., Nakagawa, M., Gilbert, A., Yoshida, N., Matsumoto, R., Sekine, Y., 2021. Doubly substituted isotopologues of methane hydrate (13CH3D and 12CH2D2): Implications for methane clumped isotope effects, source apportionments and global hydrate reservoirs. Geochim. Cosmochim. Acta 315, 127–151.